UNIVERSIDAD DE CONCEPCIÓN
FACULTAD DE CIENCIAS QUÍMICAS
PROGRAMA DE DOCTORADO EN CIENCIAS GEOLÓGICAS

APLICACIONES DEL RUIDO SÍSMICO AMBIENTAL PARA ESTUDIAR Y MONITOREAR EL TRANSPORTE Y ALMACENAMIENTO DE MAGMAS EN EL ARCO VOLCÁNICO ANDINO, CHILE

por

DIEGO M. GONZÁLEZ-VIDAL

Tesis presentada a la Facultad de Ciencias Químicas de la Universidad de Concepción para optar al grado de Doctor en Ciencias Geológicas

Profesor guía	:	Dr. Matthew Miller (Universidad de Concepción)
Comisión evaluadora	:	Dr. Marcos Moreno (Universidad de Concepción)
		Dr. Sergio Ruiz (Universidad de Chile)

Agosto de 2019

Concepción, Chile

AGRADECIMIENTOS

Esta tesis de investigación doctoral no hubiese sido posible sin el aporte de todas las personas que conocí a lo largo de estos años. En primer lugar, agradecer al Dr. Klaus Bataille por su invaluable apoyo intelectual y humano para iniciar este trabajo. También, estoy muy agradecido de las experiencias e ideas compartidas junto al Dr. Matteo Lupi, con quien tuve la oportunidad única de participar en campañas de terreno en los Andes del Sur y la costa Oeste de Grecia, una pasantía de 5 meses en la Universidad de Ginebra (Suiza) y participar en varias conferencias internacionales. También, estoy muy agradecido del gran apoyo por parte del Dr. Matthew Miller durante la etapa de pre-grado y posteriormente el doctorado. Siempre estuvo dispuesto a compartir sus códigos para el procesamiento de datos sismológicos y material docente, lo cual fue escencial en mi desarrollo como investigador. Agradezco las conversaciones, experiencias y vivencias de parte de los estudiantes del Programa de Doctorado en Ciencias Geológicas, Universidad de Concepción, así como también de sus profesores y funcionarios. Al Dr. Andrés Tassara, Dr. Jose Luis Palma, Dra. Anne Obermann, Dr. Dietrich Lange, Dr. Gerd Sielfeld, Dr. Luis Franco, Dr. Luca Guglielmetti, por las dicusiones y conversaciones constructivas que me ayudaron a desarrollar la investigación. También, agradezco a la Dra. Susan Beck, Dr. Kevin Ward y Dr. Jonathan Delph por la oportunidad de participar en un taller sobre "To-

mografía de Ruido Sísmico" en la Universidad de Arizona (Estados Unidos), 2016.

A mi familia y amig@s, muchísimas gracias. Siempre me he sentido afortunado de su apoyo incondicional.

Para finalizar, agradecer al Centro Sismológico Nacional (Chile), al Observatorio Volcanológico de los Andes del Sur (Chile), a IRIS *Data Management Center* (EEUU) y al GIPP *Geophysical Instrument Pool Potsdam* (Alemania) por compartir los datos sísmológicos y metadata que fueron utilizados en este trabajo. Este trabajo ha sido financiado por CONICYT PFCHA/BECA NACIONAL DE DOCTORADO/2015 – 21150624.

RESUMEN

La volcanología moderna tiene como desafío mostrar la naturaleza de los procesos magmáticos asociados al transporte y almacenamiento de fundidos desde el manto hasta la superficie de la Tierra. La expresión de estos fenómenos en la superficie son los diversos volcanes (o sistemas volcánicos) que existen en la Tierra, cuya morfología, evolución, tipos de erupciones y comportamiento varía ampliamente a concecuencia de las condiciones tectónicas de la región, composición de los magmas y tasa de producción de fundidos. Grandes avances en la capacidad computacional e instrumentación, así como también la integración de múltiples observaciones geofísicas, geoquímicas y petrológicas de erupciones volcánicas recientes, han permitido el desarrollo de nuevas herramientas que han ayudado a comprender en mayor detalle los procesos que condicionan el magmatismo.

En particular, el ruido sísmico ambiental ha sido ampliamente utilizado en una variedad de regiones para estudiar la estructura de la corteza y los procesos magmáticos que ocurren cerca de la superficie. En este trabajo, utilizamos dos técnicas de análisis de datos que utilizan el ruido sísmico ambiental para monitorear cambios en el nivel de actividad en sistemas volcánicos, y estudiar las estructuras geológicas que afectan su desarrollo y comportamiento en la parte superior de la corteza: "Interferometría de Ondas de Coda" y "Tomografía de Ondas Superficiales". Utilizando

datos provenientes de tres zonas de interés en Chile aplicamos el procesamiento estándar para el análisis de ruido sísmico ambiental. Nuestros resultados indican que, en sistemas volcánicos de conducto abierto como el volcán Villarrica, pequeñas perturbaciones en las propiedades elásticas del medio pueden ser detectadas antes que se vuelvan evidentes en el nivel del tremor volcánico y en la actividad observada en la superficie. También, definimos un modelo representativo de la estructura de la corteza bajo el segmento del arco volcánico comprendido desde 35,5°S a 37,5°S a partir del ruido sísmico ambiental: los magmas son transportados (y acumulados) lateral y verticalmente a través de zonas frágiles en la corteza, en donde los diques intruyen y conectan reservorios magmáticos localizados en la corteza. Nuestros resultados sugieren que grandes acumulaciones de magma ocurren aproximadamente a 5 km de profundidad y no necesariamente están localizados bajo el edificio volcánico

ABSTRACT

The challenge of modern volcanology is to show the nature of the magmatic processes associated with the transport and storage of melts from the mantle to the surface of the Earth. The expression of these phenomena on the surface are the various volcanoes (or volcanic systems) that exist on Earth, whose morphology, evolution, types of eruptions and behavior vary widely as a consequence of the tectonic conditions of the region, composition of the magmas and melt production rate. Great advances in computational and instrumentational capacity, as well as the integration of multiple geophysical, geochemical and petrological observations of recent volcanic eruptions, have allowed the development of new tools that have helped to understand in detail the processes related to magmatism.

In particular, ambient seismic noise has been widely used in a variety of regions to study the structure of the crust and the magmatic processes that occur near the surface. Here, we use two data analysis techniques that use ambient seismic noise to monitor changes in the level of activity in volcanic systems, and to study the geological structures that affect their development and behavior in the upper part of the crust: "Coda Wave Interferometry" and "Surface Wave Tomography". Using data from three regions of interest in Chile, we apply standard processing for the analysis of ambient seismic noise. Our results indicate that, in open-vent volcanoes

such as the Villarrica volcano, small perturbations in the elastic properties of the medium can be detected before they become evident in the level of the volcanic tremor and in the activity observed on the surface. Also, we define a representative model of the structure of the crust under the segment of the volcanic arc comprised from 35,5°S to 37,5°S from ambient seismic noise: the magmas are transported (and stored) laterally and vertically through fragile zones in the crust, where dykes intrude and connect magmatic reservoirs located within the crust. Our results suggest that large accumulations of magma occur approximately 5 km deep and are not necessarily located under the volcanic edifice.

Índice general

Capítulo 1

INTRODUCCIÓN

1.1. Planteamiento del problema

La Cordillera de los Andes es un lugar privilegiado para estudiar la estrecha relación que existe entre procesos de mineralización, deformación cortical y magmatismo en márgenes convergentes (López-Escobar et al., 1995; Oncken et al., 2006; Charrier et al., 2007). La subducción de la placa Nazca por debajo de la placa Sudamericana permite la fusión parcial del manto astenosférico y el ascenso de magmas hacia la parte inferior de la corteza, también conocido como zona de MASH (*Mixing, Assimilation, Storage and Homogenization*, en inglés). Desde ahí, los magmas ascienden hasta la superficie a través de intrusiones de diques que se acomodan horizontal o verticalmente a lo largo de la corteza (Tibaldi, 2008; Acocella, 2014; Lupi and Miller, 2014). El transporte y almacenamiento de magmas a través de la corteza, así como también la presencia de volcanes activos en la superficie, está condicionado principalmente por la geometría y oblicuidad de subducción, las estructuras heredadas del basamento Paleozoico, el grado de evolución de los magmas, y la configuración

tectónica local (i.e., $\lesssim 10^4$ km^2) y regional (i.e., $\gtrsim 10^5$ km^2) (Stern, 2004; Cembrano and Lara, 2009).

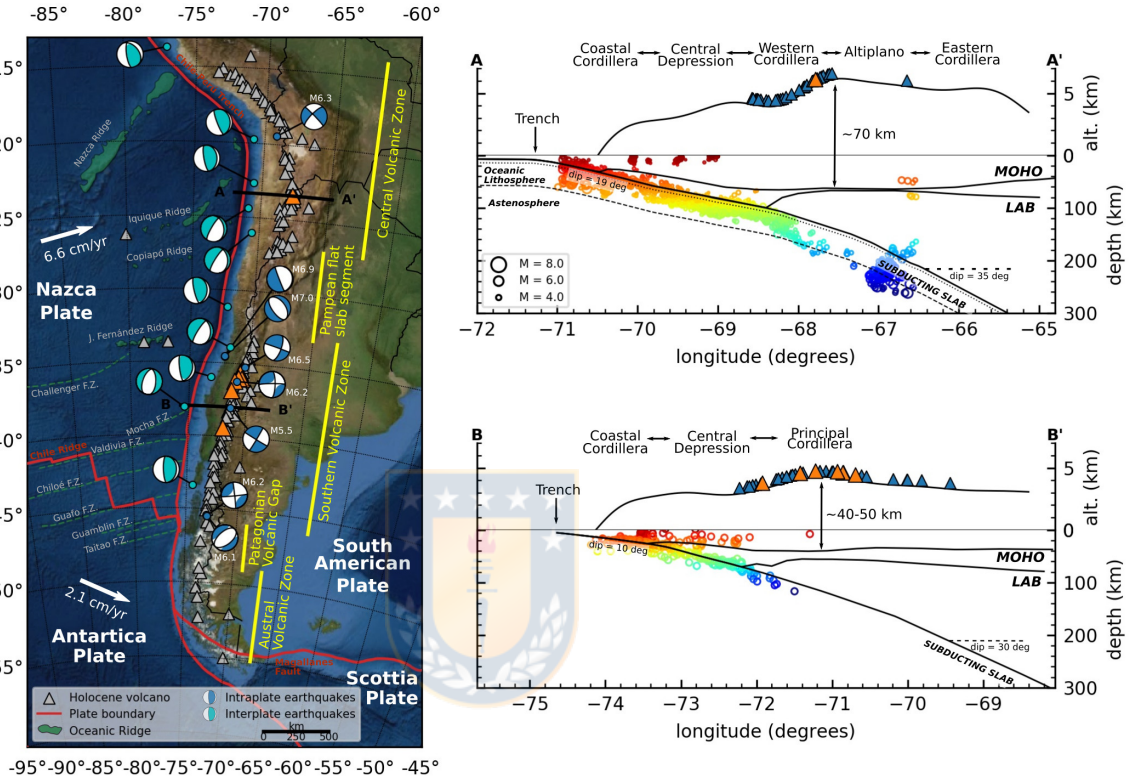

Figura 1.1: Mapa de Chile donde se destaca la configuración tectónica y distribución del arco volcánico. Los triángulos azules muestra la distribución de volcanes activos (i.e., actividad dentro de los últimos 12,000 años), mientras que los triángulos naranjos muestran los volcanes estudiados en este trabajo. Los mecanismos focales de color azul corresponden a terremotos intraplaca (Santibáñez et al., 2019) mientras que los de color celeste corresponden a terremotos interplaca (fuente gCMT, URL: *https://www.globalcmt.org*). La segmentación del arco volcánico y morfoestructuras han sido modificadas de (Stern, 2004; Charrier et al., 2007; Cembrano and Lara, 2009). Los límites del MOHO (*Mohorovic discontinuity*, en inglés) y LAB (*Litosphere-Astenosphere Boundary*, en inglés) han sido modificados de Tassara and Echaurren (2012). El MOHO está referido a la discontinuidad entre la corteza y el manto, mientras que el LAB es referido a la discontinuidad termal entre la litósfera y astenósfera. Los perfiles de sismicidad en A-A′ y B-B′ han sido modificados de Sippl et al. (2018) y Haberland et al. (2009), respectivamente. El gradiente de color está asociado a la profundidad de cada evento, mientras que el tamaño del marcador a su magnitud. El grosor de la placa oceánica en el perfil A-A′ ha sido graficado de acuerdo a los resultados obtenidos por Sodoudi et al. (2011).

En Chile, el arco volcánico se ubica aproximadamente a $250-300$ km al Este de la

fosa Chile-Perú (Fig. 1.1). A partir de las características morfológicas, geoquímicas y petrológicas de los magmas extruidos en la superficie, el arco volcánico ha sido dividido en cuatro segmentos llamados Zona Volcánica Norte ($5°N - 2°S$), Zona Volcánica Central ($14°S - 27°S$), Zona Volcánica Sur ($33°S - 46°S$) y Zona Volcánica Autral ($49°S - 55°S$). La estructura interna del sistema de subducción (i.e., límite entre la placa subductante y cabalgante, límite entre la corteza y manto, límite entre la litósfera y astenósfera, y distribución de fundidos desde el manto hasta la superficie), ha sido inferido a escala regional (i.e., $\gtrsim 10^5$ km^2) a partir de la integración múltiples modelos gravimétricos, geodésicos y termomecánicos, así como también tomografías sísmicas y eléctricas (Bohm et al., 2002; Asch et al., 2006; Yuan et al., 2006; Haberland et al., 2009; Vigny et al., 2011; Tassara and Echaurren, 2012; Ward et al., 2013; Delph et al., 2017; Sippl et al., 2018; Moreno et al., 2018). Debido a que el grosor de la corteza en el norte de Chile ($\sim$ 70 km) es superior al sur de Chile ($\sim 40-50$ km), los magmas extruídos son más diferenciados y contienen mayor contaminación cortical. En general, el transporte de magmas (o fundidos parciales) a través de la corteza ha sido evidenciado a partir de la deformación del medio alrededor del volcán, así como también cambios en la tasa de actividad sísmica y de emisión de gases hacia la atmósfera (Hill et al., 2002; Scarpa and Tilling, 2006). Sin embargo, aún se desconoce en mayor parte del arco volcánico en Chile, cual es la distribución de los magmas en la corteza a una escala local (i.e., $\lesssim 10^4$ km^2) y cuales son las estructuras geológicas que condicionan su transporte y almacenamiento.

1.2. Preguntas de investigación

Se utilizaron dos preguntas científicas para orientar esta investigación:

- ¿Cuál es la distribución espacial y temporal de los magmas bajo el arco volcánico a escala local?
- ¿Cuales son las estructuras geológicas en la corteza que condicionan el transporte y almacenamiento de magmas bajo el arco volcánico?

1.3. Objetivo general y específicos

El Objetivo General de este trabajo es monitorear la estructura de velocidades sísmicas en la vecindad de volcanes, y estudiar la distribución espacial de las estructuras geológicas que afectan el desarrollo y comportamiento del arco volcánico.

A continuación, se enumeran los Objetivos Específicos:

1. Cuantificar perturbaciones temporales en la velocidad de ondas sísmicas alrededor de un volcán, y establecer su relación con los procesos magmáticos que ocurren en la corteza.
2. Cuantificar perturbaciones espaciales en la velocidad de ondas sísmicas de un segmento del arco volcánico, y definir un modelo de la estructura interna de la corteza.

1.4. Métodos y materiales

En este trabajo se escogieron tres áreas de estudio ubicadas en Chile: el volcán Lascar, el volcán Villarrica y segmento del arco volcánico comprendido entre las latitudes 35,5°S y 37,5°S (Fig. 1.1).

1.4.1. Ruido sísmico ambiental

El ruido sísmico ambiental está compuesto principalmente por ondas superficiales de baja amplitud que se generan como la respuesta elástica de un receptor a múltiples fuentes de ruido distribuidas aleatoriamente en el espacio (Fig. 1.2A). Si el ruido sísmico ambiental es lo suficientemente coherente entonces la señal que virtualmente se propagaría entre dos receptores x_A y x_B (Campillo and Paul, 2003; Shapiro and Campillo, 2004; Wapenaar et al., 2010), se puede obtener a partir de la correlación cruzada entre las respuestas de ambos receptores a partir de:

$$\{G(x_B, x_A, t) + G(x_A, x_B, -t)\} * S_s(t) = u(x_B, x_S^{(i)}, t) * u(x_A, x_S^{(i)}, -t) \qquad (1.1)$$

Donde $*$ representa el operador de convolución temporal, $G(x_B, x_A, t)$ la función de Green, u la respuesta de un receptor (Fig. 1.2B), y $S_s(t)$ la autocorrelación de las fuentes de ruido.

Existen dos posibles aplicaciones en las cuales se puede utilizar la función de

Green (o señal virtual) obtenida a partir del ruido sísmico ambiental entre dos receptores. La primera es estudiar la coda de la señal, la cual se compone por ondas sísmicas altamente dispersadas, y se ha utilizado para cuantificar perturbaciones en los tiempos de viaje de las ondas de coda y complementar el monitoreo en (casi) tiempo real de volcanes activos (Brenguier et al., 2008, 2011; Sens-Schönfelder and Wegler, 2011). La segunda aplicación es calcular la dispersión y tiempos de viaje de la onda superficial que viaja (virtualmente) entre múltiples receptores, para luego visualizar la estructura sísmica de la corteza a partir de una "Tomografía de Ondas Superficiales" (Shapiro et al., 2005; Brenguier et al., 2007; Snieder and Wapenaar, 2010).

Una de las grandes ventajas que tiene el análisis del ruido sísmico ambiental por sobre los métodos tradicionales es que el ruido no depende del hipocentro de la fuente sísmica y puede ser registrado contínuamente desde cualquier lugar de la Tierra. También, es sensible a perturbaciones en la velocidad de ondas sísmicas del orden de $\sim 0{,}1\,\%$ en la corteza. Además, la resolución espacial de las imágenes tomográficas es mayor a la obtenida por los métodos tradicionales (Yang and Ritzwoller, 2008). Sin embargo, existen limitaciones asociadas a la geometría de la red de estaciones sísmicas, y a la continuidad y de datos registrados. En los capítulos 2, 3 y 4 se ampliarán los detalles sobre las metodologías asociadas al análisis del ruido sísmico ambiental.

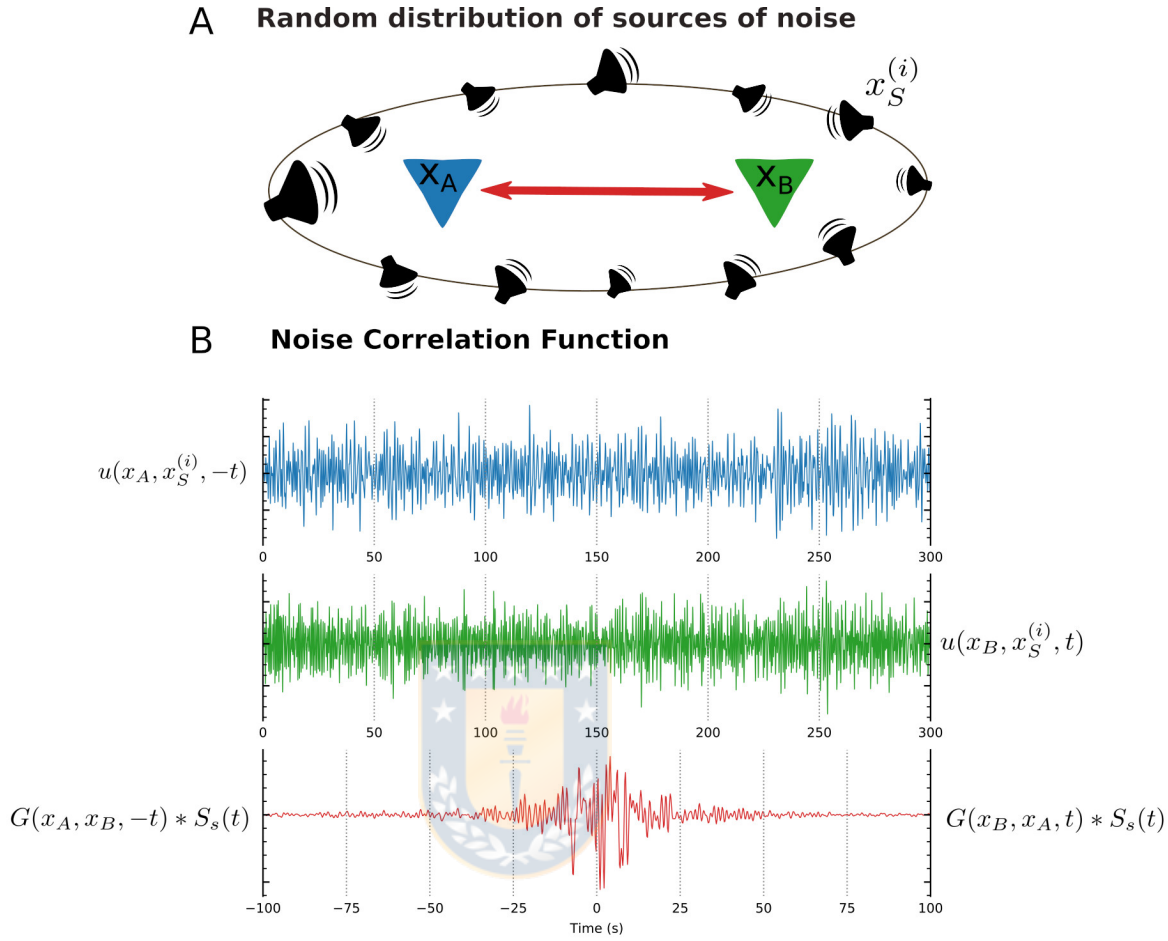

Figura 1.2: (A) Representación esquemática de la distribución aleatoria de múltiples fuentes de ruido ($x_S^{(i)}$) alrededor de dos receptores (x_A y x_B). (B) Respuesta elástica del receptor x_A y x_B (línea azul y verde, respectivamente), y función de Green obtenida a partir de la correlación cruzada de las respuestas de ambos sensores (línea roja).

1.4.2. Base de datos sísmicos

Se compiló una base de datos sísmicos provenientes de las redes permanentes del Centro Sismológico Nacional (CNS)[1] y del Observatorio Volcanológico de los Andes del Sur (OVDAS)[2], de la red temporal *Southern Andes Intra-Arc seismicity project*

[1]https://www.csn.uchile.cl/
[2]https://www.sernageomin.cl/red-nacional-de-vigilancia-volcanica/

(SAIAS)[3], y de la red temporal GeoTeam[4]. Mayor información de la red temporal GeoTeam en el Apéndice A.

En el Capítulo 2, se utilizaron datos de la red permanente de OVDAS ubicada alrededor del volcán Láscar (Fig. 1.3A). La red consiste en 5 sismómetros banda ancha Reftek 151-30 s que registraron datos desde Febrero hasta Julio de 2013. En el Capítulo 3, se utilizaron datos de 3 sismómetros banda ancha Reftek 151-30 s, 2 sismómetros banda ancha Trillium 120 s y 4 sismómetros periodo corto Mark L4-3D, provenientes de la red SAIAS y OVDAS. Las estaciones sísmicas estuvieron registrando datos desde Abril de 2014 a Junio de 2015 y ubicadas a menos de 25 km del volcán Villarrica (Fig. 1.3B). En el Capítulo 4 se utilizaron datos de 15 sismómetros banda ancha Trillium 120 s provenientes de la red permanente del CSN y 21 estaciones temporales provenientes de la red GeoTeam. La red GeoTeam estuvo compuesta por 11 sismómetros banda ancha Guralp ESP-C y 10 sismómetros periodo corto Mark L4C (Fig. 1.3C). La red se ubicó en el segmento del arco volcánico desde 35,5°S hasta 37,5°S y registró datos desde Noviembre de 2013 hasta Marzo de 2015. La localización de todas las estaciones sísmicas se encuentra en el Cuadro 1.1.

[3]https://gipp.gfz-potsdam.de/webapp/projects/view/240
[4]https://gipp.gfz-potsdam.de/webapp/projects/view/248

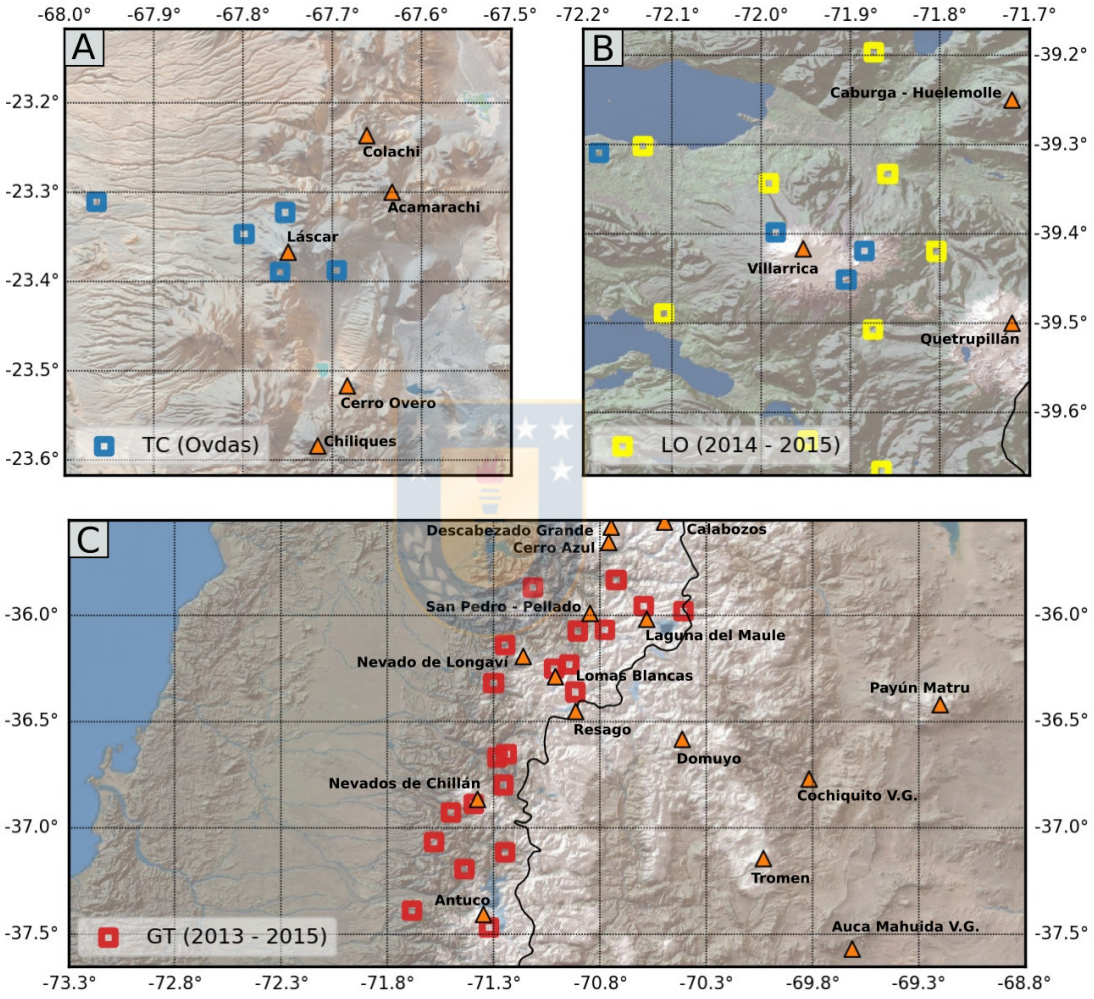

Figura 1.3: Estaciones sísmicas que proporcionaron los datos utilizados en (A) el Capítulo 2, (B) el Capítulo 3 y (C) el Capítulo 4. TC es la red permanente de estaciones sísmicas de OVDAS (Sernageomin, Chile). LO y GT son redes temporales de estaciones sísmicas facilitadas por el GIPP (*Geophysical Instruments Pool Potsdam*, en inglés).

Red	Estación	Longitud (°)	Latitud (°)	Red	Estación	Longitud (°)	Latitud (°)
		CAPÍTULO 2		GT	BB07	-70.4067	-35.9816
TC	TAL	-67.9470	-23.3110	GT	BB08	-70.5937	-35.9582
TC	PUN	-67.7418	-23.3896	GT	BB09	-70.9056	-36.0740
TC	QUE	-67.7364	-23.3228	GT	BB10	-70.9443	-36.2322
TC	LAS	-67.7820	-23.3470	GT	BB11	-70.9161	-36.3607
TC	LEJ	-67.6782	-23.3874	GT	SP01	-71.2806	-36.6679
		CAPÍTULO 3		GT	SP02	-71.5016	-36.9267
LO	LS4S	-71.8540	-39.1966	GT	SP03	-71.6851	-37.3882
LO	LZ1B	-71.9276	-39.6313	GT	SP04	-71.2445	-36.1410
LO	LV6B	-71.5498	-39.4771	GT	SP05	-71.5811	-37.0680
LO	LV2S	-71.8383	-39.3330	GT	SP06	-71.2399	-36.6532
LO	LS6S	-71.5748	-39.3625	GT	SP07	-70.7754	-36.0699
LO	LV7S	-72.0888	-39.4888	GT	SP08	-71.2523	-36.7983
LO	LZ2S	-71.8453	-39.6650	GT	SP09	-71.2462	-37.1146
LO	LV8B	-71.8545	-39.5068	GT	SP10	-71.0147	-36.2508
LO	LZ3S	-71.7541	-39.7745	C1	BI02	-71.2731	-36.6634
LO	LV1S	-72.1125	-39.3013	C1	BI03	-73.0258	-36.8438
LO	LV3R	-71.9713	-39.3431	C1	BO01	-71.0848	-34.3917
LO	LV4B	-71.7835	-39.4196	C1	BO02	-70.7814	-34.7924
LO	LS5R	-71.6131	-39.2146	C1	LC01	-71.8761	-38.8975
TC	VN2	-71.9637	-39.3985	C1	MT01	-71.2509	-33.8641
TC	TRA	-71.8847	-39.4513	C1	MT02	-71.1377	-33.2591
TC	KIK	-71.8645	-39.4191	C	GO05	-71.9303	-35.0099
TC	CVV	-72.1617	-39.3091	C	GO06	-71.4720	-39.5839
		CAPÍTULO 4		G	PEL	-70.6749	-33.1436
GT	BB01	-71.3202	-37.4672	IU	TRQA	-61.9787	-38.0568
GT	BB02	-71.2999	-36.3204	GT	PLCA	-70.5508	-40.7328
GT	BB03	-71.3931	-36.8886	C1	VA01	-71.6374	-33.0229
GT	BB04	-71.1141	-35.8686	C1	MT05	-70.7381	-33.3919
GT	BB05	-71.4354	-37.1934	C1	MT03	-70.5102	-33.4936
GT	BB06	-70.7232	-35.8334				

Cuadro 1.1: Localización de estaciones sísmicas utilizadas en este trabajo.

Capítulo 2

TEMPORAL SEISMIC WAVE VELOCITY VARIATIONS AT LÁSCAR VOLCANO

Abstract

We report on the first study using Seismic Wave Interferometry to determine variations of seismic velocities through time, in the vicinity of Lascar volcano in Chile. Seismic Wave Interferometry has been used as a powerful tool to determine spatial and temporal changes of seismic velocities within the Earth. Spatial variations of seismic velocities are related to heterogeneities of material properties, which are expected to occur in a complex structure. However, temporal changes are indicative of dynamic process within the elastic media, and thus, this tool can be used to monitor dynamic processes at volcanic zones. We find consistent variations on three stations close to the volcano, with dv/v of $\pm 0{,}6\,\%$, most likely related to the inflation / deflation process due to fluid movement of magmatic or hydrothermal origin within the volcanic structure. During the observed period of velocity variation, OVDAS reported an increase of volcanic activity evidenced by the increase of the

number of Long Period seismic events, increase of gas emissions and the formation of incandescence above the crater. We suggest that this tool can contribute to the understanding of volcano related dynamic processes, as well as for routine volcano monitoring purposes.

Published as: González-Vidal D.; Bataille, K.; Eulendeld, T.; Franco, L.E. (2016), Temporal seismic wave velocity variations at Láscar volcano, *Andean Geology, 43 (2), 240-246.*

2.1. Introduction

Lascar is a stratovolcano located at 23,95°S, 67,88°W, and 5592 meters of altitude, at approximately 350 km from the trench separating the Nazca and South American plates (Figure 2.1). It has been active since at least 50 ka. Its recent activity is characterized by the continuous emission of gases and occasional sub-plininians eruptions, as in April 1993. In 2006, the Observatorio Volcanológico de los Andes del Sur (OVDAS) reported an increase of activity characterized by a plume emitted by the main cone, up to an altitude of 3000 above the crater. Most recently, between March and April 2013, OVDAS reported an increment of the number of seismic Long Period events, together with a degasification process and incandescence near the crater of Lascar volcano.

Due to the availability of seismic data from 5 broad band stations, near the crater, it poses an opportunity to test if with Seismic Wave Interferometry it is possible to detect changes of velocity around the volcano. If it is possible, it would contribute towards the understanding of the associated processes and could become a tool for monitoring purposes.

Seismic Wave Interferometry is based upon the concept that ambient noise, originating everywhere throughout the Earth's surface, acts as a continuous source of waves propagating along every possible direction. When considering a pair of stations, the crosscorrelation of their signals produces constructive interference for

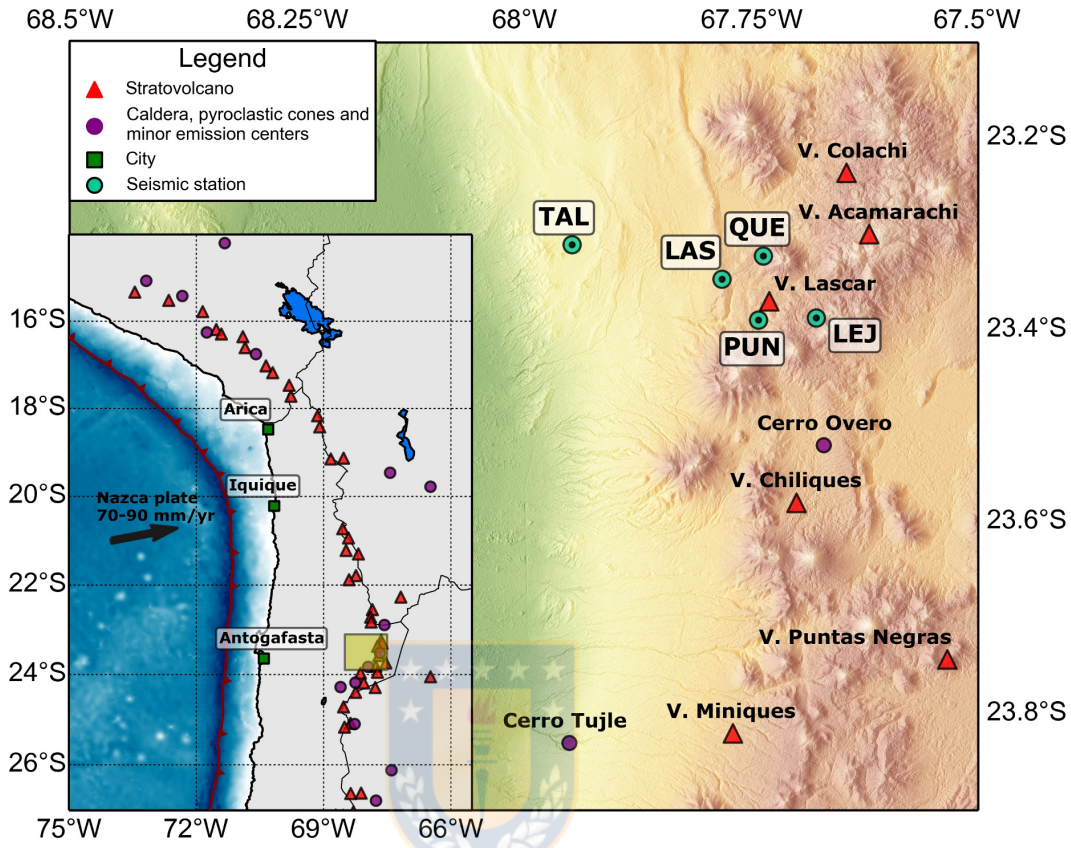

Figura 2.1: Map showing the active centers within the Southern Central Andes Volcanic Zone. The study area is shown within the yellow box where Lascar volcano is located (23,37°S - 67,73°W). Seismic stations are shown with their codes, where distances to the crater varies between 2,7 km (PUN) and 22 km (TAL).

waves propagating along the great circle path between both stations, and destructive interference among all others paths. Therefore, considering long lapse times, the cross-correlation signal between two stations becomes an empirical Green's function for a virtual source located at one station and recorded at the other. The Green's function includes the main wave and its coda. The coda represents the contribution of waves originating at the virtual station and being scattered in its vicinity before arriving at the other station. Slight waveform variations through time along the coda, or stretching, is due to variations of seismic velocity through time within the

volume between both stations.

The Seismic Wave Interferometry methodology consist in quantifying the stretching within the coda, giving the amount seismic velocity variation through time (Campillo, 2006; Snieder, 2006). This methodology has been applied to several volcanic centers worldwide. For instance, at the Piton de la Fournaise volcano, in La Reunion Island, a decrease of 0,1 % of seismic velocities before eruptions were observed (Brenguier et al., 2011). At the Merapi volcano, Sens-Schönfelder and Wegler, 2006, observed a strong seasonal variation of seismic velocities, and modelled as due to a hydrological effect. Since OVDAS is monitoring several volcanic centers in Chile, we asked if this methodology can contribute towards monitoring velocity changes around these volcanoes, by testing on specific case, namely Lascar.

2.2. Data and processing

Lascar volcano is being monitored since 2013, by OVDAS, with 5 broad band stations (Figure 2.1), recording at 100 samples per second. Stations LAS and QUE are located at approximately 4,5 km from the crater, LEJ at 5,5 km, PUN at 2,5 and TAL at 20 km. Here we use vertical components between the period of February 12 to July 11, 2013. We remove the instrumental response and resample at 50 Hz.

We first generate time series of 1 day duration, and use a 1-bit normalization filter in amplitude to eliminate the presence of seismic events (Shapiro and Campillo, 2004; Bensen et al., 2007). We then calculate the crosscorrelation between all pair of

stations, and autocorrelation for all stations. The crosscorrelation can be considered as the Green's function where one source acts as a virtual source (Wapenaar et al., 2010). For the autocorrelation, the virtual source is located at the same station. In this case, the coda generated is due to scattering within a volume surrounding the station. Therefore, velocity variations occurring in a region close to a station, would affect both the autocorrelation and crosscorrelations associated to such station.

The range of frequencies to use depends directly on the geometry of the network, and the object of study. Sens-Schönfelder (2008), suggests to use low frequencies for crosscorrelations, due to interference generated by high frequencies on the far field. In our case we concentrate on the $0{,}3 - 6$ Hz band for crosscorrelations and $4 - 6$ Hz for autocorrelations.

Once the correlation functions are obtained for each day, during the complete period of 6 months, we stack them to obtain the average correlation function for such period. The main feature of the average crosscorrelation, is the surface wave propagating at an average velocity of $v_s = 4{,}2$ km/s. To the daily correlation function we subtract the average correlation function, to identify anomalous features through time.

Slight changes of seismic velocities during the period of observation, would produce slight variations of the coda within such period. If there is an slight decrease/increase of seismic velocity in a region, waves passing through this region will be stretched like an accordion, increasing/decreasing the period of waveforms. Seismic

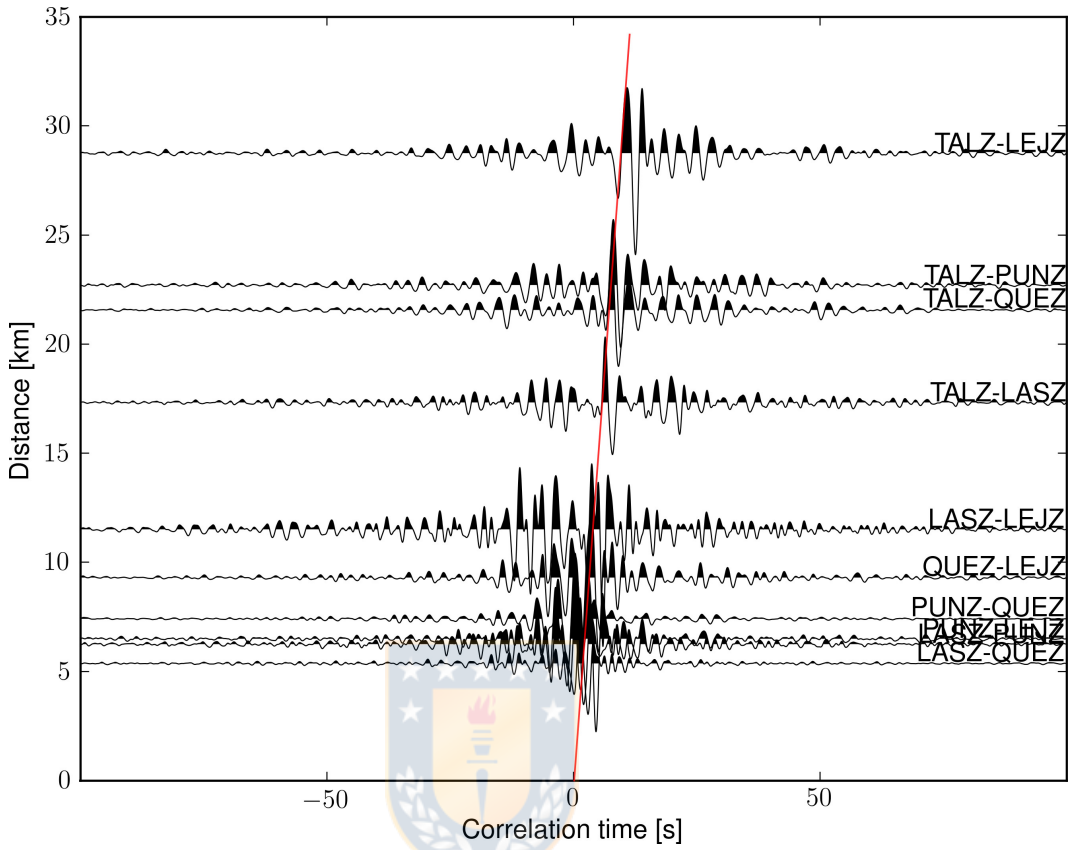

Figura 2.2: Crosscorrelation function for each pair of stations, obtained from ambient noise during 149 continuous days. Signal is filtered for periods between $1 - 20$ s. The red line shows the average propagation velocity of $v_s = 4{,}2$ km/s.

Wave Interferometry concentrates on the analysis of the coda, to identify such waveform variations, calculating the amount of stretching, dt/t (Snieder, 2006). The amount of stretching is obtained by modeling the waveforms for different stretching factors, and choosing the one with the highest correlation factor R between model and observations. Here we select values of stretching only when the correlation function $R > 0{,}8$. Knowing the stretching factor dt/t, the velocity change through the region is given by $dv/v = -dt/t$.

The source of waves within the coda of the correlation function, are waves scat-

tered in the vicinity of the involved stations. The longer the time within the coda, the larger the region involved. Here we choose windows of $5 - 10$ s and $5 - 7$ s, representing roughly a volume of $10 - 15$ km radius, which is expected to be the region most affected by volcano processes.

2.3. Results and Discussion

Our main result is the calculated stretching factor dt/t shown in Figures 2.4 y 2.5 for cross- and auto-correlations. Blue dots indicate the stretching values with the highest correlation factors R (for $R > 0{,}8$). The are common features on the observed velocity variation through time, obtained from the cross- and auto-correlation for different stations, as shown in Figure 2.6. If these features are due to a real phenomenon, and not to a processing artifact, then, it would prove to be a powerful tool for studying volcanic processes near volcanoes, and also serve as a monitoring tool. Among these common features one can observe a period between March and April 2013, with an abrupt increase of velocity ($\sim 0{,}6\,\%$ at QUE station) followed by a slow decrease. These changes could be due to a deflation process followed by an inflation process related to a loading and unloading of a hydrothermal and/or magmatic system beneath the Lascar volcano.

It is difficult at this stage, and without strong independent evidence, to state that these features are a real phenomenon. However, it is reasonable to expect the presence of fluids near the crater of an active volcano. These fluids can move due to

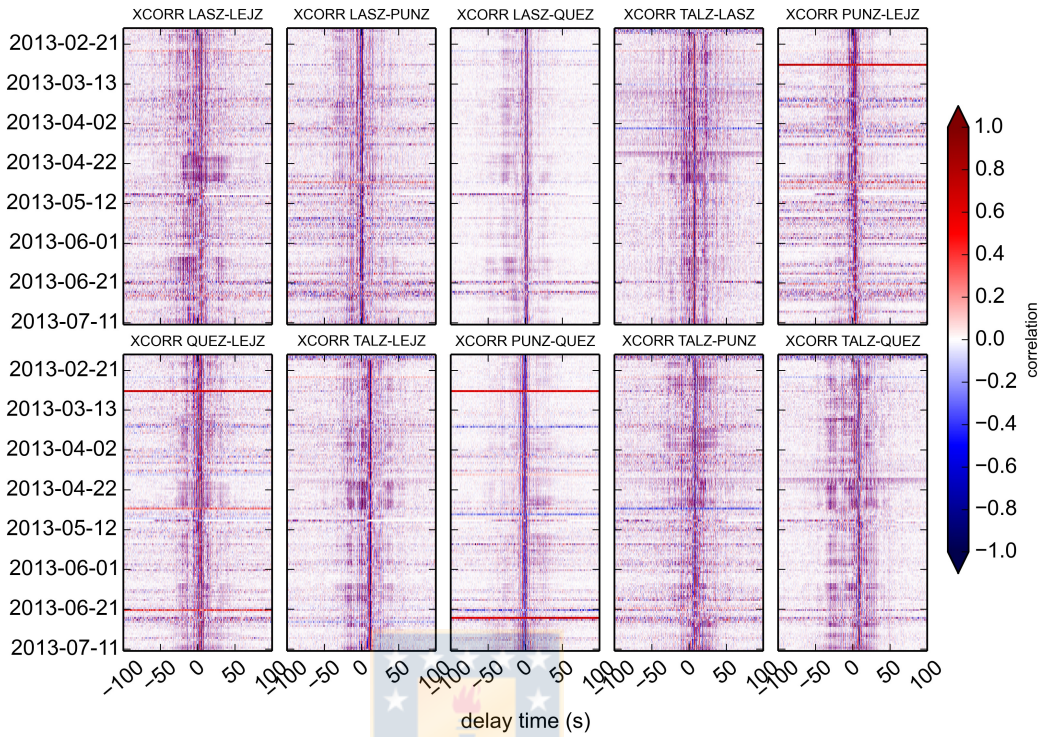

Figura 2.3: Daily crosscorrelation function for each pair of stations, between February 12 and July 11, 2013. Signals were filtered with bandpass filter between $0{,}3 - 6{,}0$ Hz and 1-bit normalization filter.

complex interactions between magma chambers and/or hydrothermal sources. The increase or decrease of the amount of fluids in the media, will produce changes in the average seismic velocity, which can be detected by seismic waves passing through these regions. Changes of velocity of the order of less than 1 % can not be detected measuring the variations of the arrival time of main seismic phases. However, these changes of velocity are capable to deform the waveform of high frequency seismic waves, in a way that can be modeled by the stretching of waveforms within the high frequency coda. The variation of seismic velocities due to the presence of fluids has been shown by Sens-Schönfelder (2008), at Merapi volcano, using this same

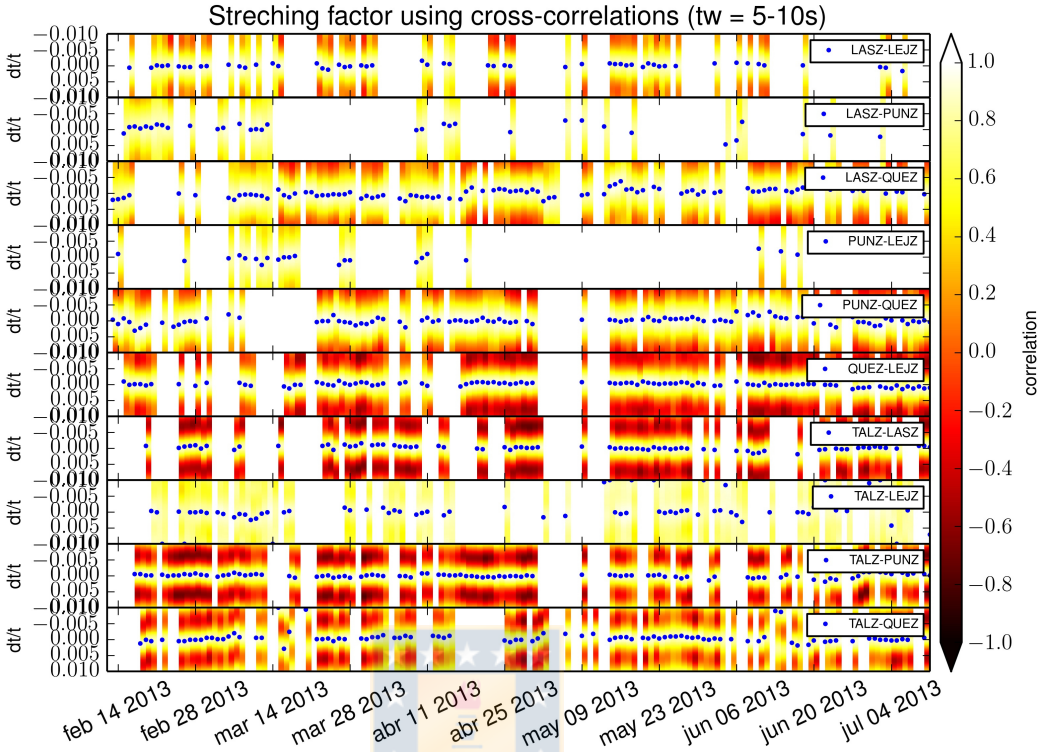

Figura 2.4: Stretching factor ($-dv/v = dt/t$) obtained from the crosscorrelation filtered between $0{,}3 - 6{,}0$ Hz, for each pair of stations. Blue dots refers to stretching factors (or velocity changes) with the highest correlation with respect to the reference trace. Only correlations with values of $R > 0{,}8$ are considered.

technique.

If our observations are due to a real phenomenon, in the following we speculate if it can be related to other inferred processes.

The deformation of the crust is sensitive to processes within, including the migration of fluids. In the past decade a great progress has been made with geodetic measurements, especially near volcanoes. However, it has been shown using InSAR that the deformation near Lascar volcano is considerable less than other zones within the Andes (Pritchard and Simons, 2004; Fournier et al., 2010; Henderson and

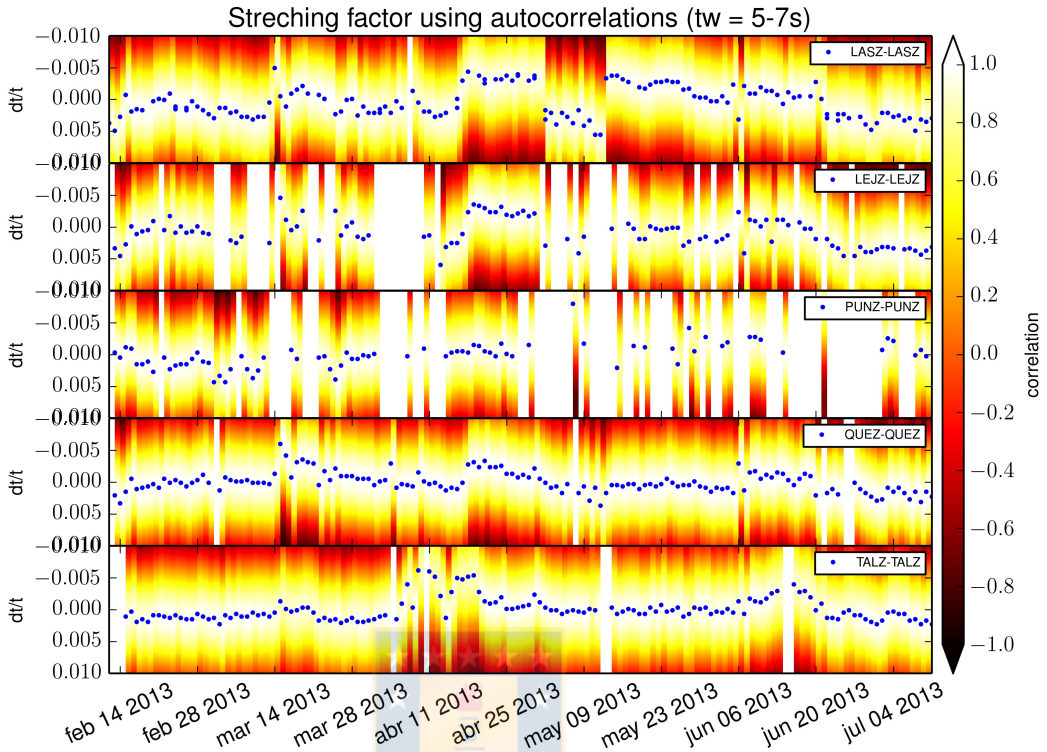

Figura 2.5: Stretching factor ($-dv/v = dt/t$) obtained from the autocorrelation filtered between $4 - 6$ Hz, for each station. Blue dots refers to stretching factors (or velocity changes) with the highest correlation with respect to the reference trace. Only correlations with values of $R > 0{,}8$ are considered.

Pritchard, 2013). Therefore, it is likely that the source of the inferred velocity change can be due to fluid motion in a very local region, and by small amounts, and can not be detected on a larger scale as observed with InSAR.

On smaller scales, studies using Magnetotelluric (Díaz et al., 2012), suggest the presence of hydrothermal source at a depth of 1 km slightly to the south of the crater. This can clearly affect seismic velocities, but within a small region, therefore it is an interesting possibility.

There are seismic studies related to the Lascar eruption in 1994-1995 (Hellweg,

1999), suggesting the presence of fluids due to complex and time varying frequencies of tremors. However, with these observations it was not possible to infer the location or geometry of the region with fluids. Another interesting analysis related to the eruption of 1994-1995, was done by Pavez et al. (2006), using InSAR images, inferring a subsidence of 17 mm near the crater. This subsidence was modeled by Pavez et al. (2006) as due to a volume change of $2 \times 10^3 \mathrm{m}^3$, of a spherical source located at 180 m below the crater. This is a very local source, and difficult to find a relation with the source of fluid motion 20 years later.

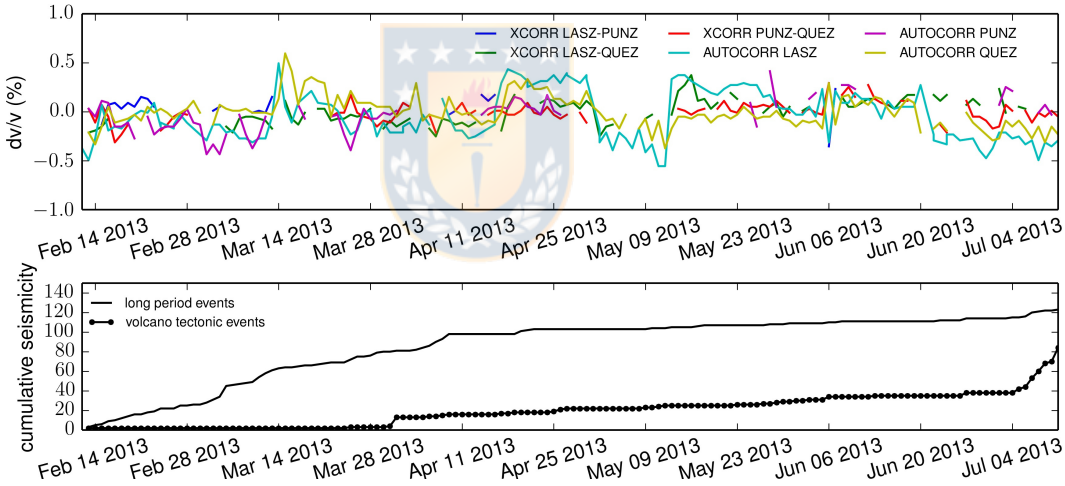

Figura 2.6: Seismic velocity change at Lascar volcano, combining cross and auto-correlations from Figures 2.4 and 2.5. Black lines show the accumulative number of LP (continuous) and VT (dotted) events.

2.4. Conclusions

We use Seismic Wave Interferometry to determine variations of seismic velocities through time, in the vicinity of Lascar volcano in Chile. We find consistent variations

on three stations close to the volcano, with dv/v of $\pm 0{,}6\,\%$, most likely related to the inflation / deflation process due to fluid movement of magmatic or hydrothermal origin within the volcanic structure. During the observed period of velocity variation, OVDAS reported an increase of volcanic activity evidenced by the increase of the number of Long Period seismic events, increase of gas emissions and the formation of incandescence above the crater. We suggest that this tool can contribute to the understanding of volcano related dynamic processes, as well as for routine volcano monitoring purposes.

Capítulo 3

PRECURSORS OF THE VILLARRICA VOLCANO (CHILE) ERUPTION ON MARCH 3rd, 2015 REVEALED BY AMBIENT SEISMIC NOISE

Abstract

The identification of a possible preparatory phase of a volcanic eruption is of utter importance for volcano monitoring and risk management. In particular, the unrest period during February 2015 and subsequent paroxysmal eruption on March 3rd, 2015 at Villarrica volcano (Chile) is an ideal case study to explore new techniques for volcano monitoring. Here, we use the ambient seismic noise technique to identify preparatory phase signals and to observe transient behavior in scattering during the pre-, syn- and post-eruption phases. We found significant seismic velocity perturbations and low waveform coherence of strongly scattered coda waves occu-

rring during times of changes in the amplitude of volcanic tremor and observations of volcanic activity at the crater (i.e., lava lake level and outgassing activity). Our results suggest that changes within a deep part of the plumbing system could have been detected before they became evident by other monitoring techniques and observations of the activity in the crater. We propose that at basaltic open-vent systems such as Villarrica, the ambient seismic noise technique could be used as a complementary monitoring tool and possibly provides more evidence of variations in the activity prior to an eruption.

Submited to *Journal of Volcanological and Geothermal Research* as: González-Vidal, D.; Palma, J.L.; Lange, D.; Sielfeld, G.; Cembrano, J.; Miller, M. Precursors of the Villarrica volcano (Chile) eruption on March 3rd, 2015 revealed by ambient seismic noise.

3.1. Introduction

Villarrica volcano is the most active volcano in the Southern Volcanic Zone, Chile (Fig. 3.1). Villarrica is a late Holocene stratovolcano built on top of a late Pleistocene collapsed caldera (López-Escobar et al., 1995; Stern, 2004) and has a glacier larger than > 30 km^2 on the south-eastern flank of the cone (Brock et al., 2007; Rivera et al., 2015). Lahars are one of the most threatening hazards (e.g., Naranjo and Lara, 2004) which can be generated from melted ice and snow during an eruption. During the last 600 years, Villarrica volcano has produced thirty three eruptions posing a constant risk for local towns and life (Van Daele et al., 2014). The composition of lavas and pyroclastic deposits erupted from the volcano is mainly basaltic andesite (Witter et al., 2004). The inter-eruptive behavior of Villarrica is characterized by open vent activity, including low-frequency events that can be associated with gas emissions, seismic tremor and a small amount of volcano-tectonic earthquakes (Witter et al., 2004; Richardson and Waite, 2013). A gas plume has persisted for decades along with a visible lava lake showing passive and mild explosive outgassing (Palma et al., 2008), which is occasionally interrupted by explosive eruptions at intervals of every few decades on average (Petit-Breuilh and Lobato, 1994; Johnson et al., 2018).

At Villarrica it has been shown that the level of activity correlates with the amplitude of the seismic tremor, mostly generated at the summit, as well as with gas emission rates and infrasound measurements (Palma et al., 2008; Richardson

and Waite, 2013; Johnson et al., 2018). Within the crater, changes in the level of activity are represented by variations in the lava-lake depth and outgassing style, and reflect changes in the amount of volatile-rich magma and gas concentrations at depth that ascend to the surface through a convective flow system (Palma et al., 2011; Aiuppa et al., 2017). The amplitude of the seismic tremor is thus used as a proxy for the level of volcanic activity at the surface, which responds to variations in magma dynamics at depth within the plumbing system. The last eruption of Villarrica on March 3rd, 2015, exhibited changes in the explosive activity at the crater (Johnson et al., 2018) that were associated with the intrusion of CO_2-rich magma, possible related to a deep intrusion of a more primitive magma (Aiuppa et al., 2017). These characteristics make Villarrica volcano an ideal case study for investigating whether the ambient seismic noise technique can used to detect subtle variations in magma dynamics at depth.

The eruption of Villarrica volcano on March 3rd, 2015 (06:01h UTC) provides a unique opportunity to explore the potential of ambient seismic noise to monitor the changes in ambient noise during the pre-, syn- and post-eruption phase at Villarrica volcano. Aiuppa et al. (2017) and Johnson et al. (2018) showed that the eruption was preceded by one month of a continuous increment of the volcanic tremor amplitude (Fig. 3.3), and anomalous CO_2/SO_2 ratios in the gas emissions. Prior to the eruption, the number, style, and intensity of the Strombolian explosions in its crater varied with time, and the level of the lava lake remained at only a few tens of meters

from the crater rim. Two days prior to the eruption of March 3rd, the Volcano Observatory of Southern Andes[1] (OVDAS/SERNAGEOMIN) prompted an "orange" alert following an increase in the frequency and intensity of the Strombolian activity taking place on the lava lake of Villarrica volcano. The eruption produced a 1500 m high lava fountain, scoria flows, lahars, avalanches made of a mixture of spatter and ice, small lava flows, tephra fall to the east of the volcano, and lightning, among other phenomena (Johnson et al., 2018). After the paroxysmal eruption, the outgassing activity ceased but quickly started to increase, and by March 17th Strombolian explosions and small lava fountains were seen again at the crater. A post-eruptive ground uplift of $4-6$ cm was observed 5 km to the SE of the volcano between mid-April and mid-May 2015 (Delgado et al., 2017). Also an intense seismic sequence occurred forty five days after the eruption at approximately 9 km depth and south-east of the eruptive vent (Sielfeld et al., 2019). Despite the intense seismic sequence and ground deformation detected after the eruption, no evident precursory activity could be linked to the eruption and more detailed studies are needed to understand the processes occurring at depth.

The main goal of this work is to identify preparatory phase signals and to observe transient behaviour in scattering during the pre-, syn- and post-eruption phase. Our results suggest that changes beneath the Villarrica eruption in 2015 could have been detected before they become evident on the surface. We propose that at basaltic

[1]URL: `http://www.sernageomin.cl/red-nacional-de-vigilancia-volcanica/`

open-vent systems such as Villarrica, the ambient seismic noise technique could be used as a complementary monitoring tool and possibly provides more evidence of changes in the activity prior to an eruption.

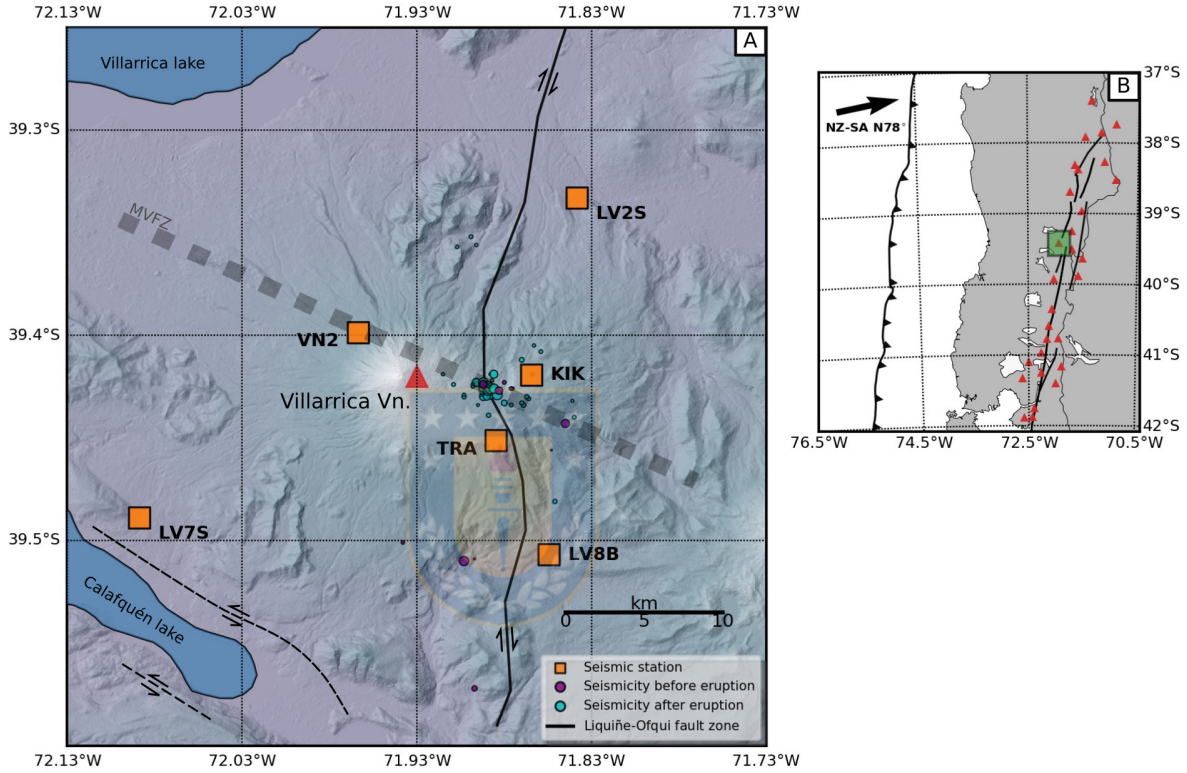

Figura 3.1: Panel A shows the topography of the region around Villarrica volcano (green square in panel B). Seismic stations are indicated with orange squares. Red triangles mark the location of Holocene volcanoes. Crustal seismicity (< 15 km depth) recorded between April 2014 and June 2015 is marked with circles (Sielfeld et al., 2019). Purple/cyan circles denote seismicity before/after the eruption on March 3rd, 2015. The Liquiñe-Ofqui Fault System is marked by a black line (Melnick and Echtler, 2006). Dashed black lines mark the sinestral-reverse strike-slip faults modified from Sánchez et al. (2013). The MFVZ is refered to location of the Mocha-Villarrica Fault Zone. The reader is referred to Sánchez et al. (2013) for futher information about the MFVZ. Panel B shows the location of the volcano in south-central Chile together with Holocene volcanoes (red triangles) and the Liquiñe-Ofqui Fault System (Melnick and Echtler, 2006) is shown with a black line. Plate convergence vector from Cembrano and Lara (2009).

3.2. Methods

The analysis of ambient seismic noise has been widely used for monitoring the Earth's interior (Grêt, 2003; Brenguier et al., 2008; Hadziioannou et al., 2011; Weaver et al., 2011; Nakata et al., 2012, 2013). Contrary to the traditional sources of seismic signals, we can extract the coherent part of ambient seismic noise between two seismic stations from the background noise caused by ocean waves, wind, volcanic tremor or even traffic. The method called Coda Wave Interferometry (CWI) compares coda waveforms from multiple scattered waves that are highly sensitive to small perturbations in seismic velocities at crustal depths (Aki and Chouet, 1975; Pacheco and Snieder, 2005; Sens-Schönfelder and Wegler, 2011; Colombi et al., 2014; Margerin et al., 2016). In particular, Duputel et al. (2008) retrieved seismic velocity perturbations using CWI from ambient seismic noise to forecast eruption and constrain the processes taking place in the volcanic plumbing system at the Piton de la Fournaise volcano (La Réunion). Such seismic velocity perturbations have been related to precursors of other volcanic eruptions at Piton de la Fournaise volcano, La Réunion (Brenguier et al., 2011; Obermann et al., 2013; Sens-Schönfelder et al., 2014; Rivet et al., 2015); Arenal volcano, Costa Rica (Snieder and Hagerty, 2004); Mt. Ruapehu, New Zealand (Mordret et al., 2010); Kilauea volcano, Hawaií (Ballmer et al., 2013; Donaldson et al., 2017); Okmok volcano, Alaska (Bennington et al., 2015); and Hakone volcano, Japan (Yukutake et al., 2016). Also, it has been

shown that CWI is useful to monitor large magnitude earthquakes (Brenguier et al., 2008; Hobiger et al., 2014; Obermann et al., 2014; D'Hour, 2015; Gassenmeier et al., 2016; Nimiya et al., 2017), landslides (Mainsant et al., 2012; Olivier et al., 2017), annual climate variations (Sens-Schönfelder and Wegler, 2006; Brooks et al., 2009; Sens-Schönfelder and Wegler, 2011; Kimman et al., 2012; Hillers et al., 2015; Lepore et al., 2016), glacier ice melt (Mordret et al., 2016), and groundwater content (Behr et al., 2013; Hillers et al., 2015; Larose et al., 2015; Lecocq et al., 2017; Clements and Denolle, 2018).

3.2.1. Seismic data

We use seismic data of three Reftek 151-30 s and two Trillium 120 s broadband seismometers, and four short period seismometers (Mark L4-3D), from the SAIAS (Southern Andes Intra-Arc seismicity project) and OVDAS/SERNAGEOMIN seismic networks (Fig. 3.1). The seismic stations were installed between April 2014 and June 2015 within 25 km around Villarrica volcano (Fig. 3.2). To optimize the use of computational resources we resampled the seismic data from 100 Hz down to 20 Hz.

The volcanic tremor is the most common type of seismic activity at Villarrica volcano (Ortiz et al., 2003). It is a continuous, irregular and low-amplitude seismic signal and is related to constant degassing or explosive events (Palma et al., 2008; Richardson and Waite, 2013). The seismic waveforms recorded by stations located near the volcanic edifice are characterized by continuous energy peaks between fre-

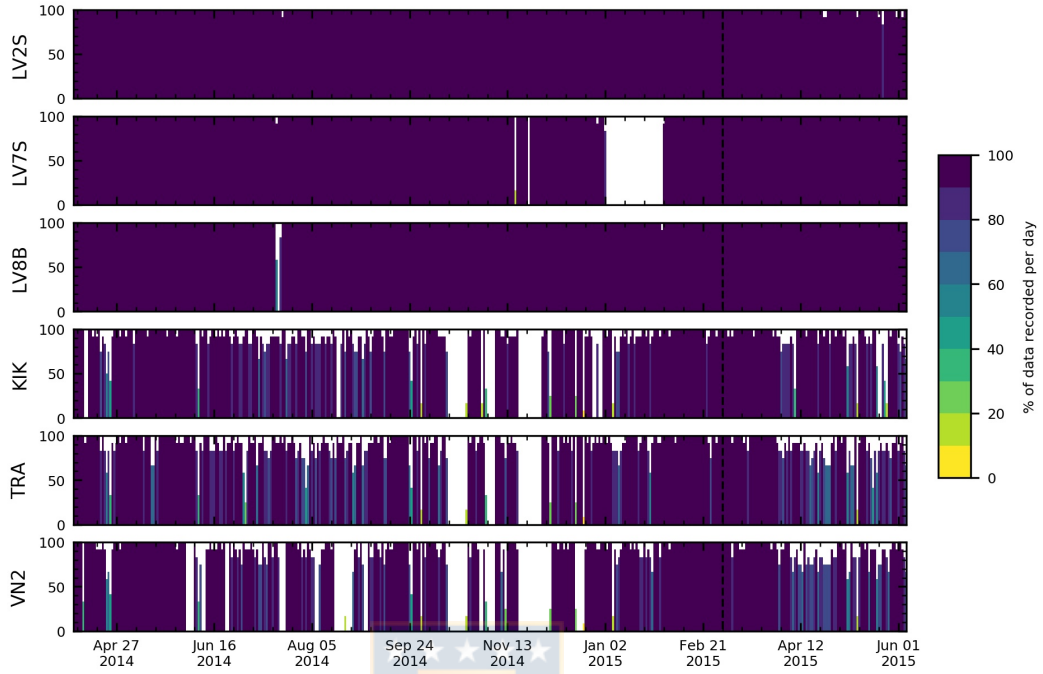

Figura 3.2: Percentage of data recorded per day for each station used in this study. Dashed vertical line mark the eruption of Villarrica volcano occurred on March 3rd, 2015.

quency bands of $0{,}1 - 0{,}3$ Hz and $1{,}2 - 2{,}5$ Hz (black arrows in Fig. 3.3B). While the energy peak of the first frequency band (i.e., $0{,}1 - 0{,}3$ Hz) is related to the oceanic microseismicity on the forearc, the second frequency band (i.e., $1{,}2 - 2{,}5$ Hz) is related to the volcanic tremor signal of Villarrica volcano (Richardson and Waite, 2013; Johnson et al., 2018). The volcanic tremor shows an anomalously high amplitude on February 6th and sustained amplitudes above background continue until the eruption on March 3rd (dashed black lines in Fig. 3.3). Note that the largest increase in energy of the volcanic tremor occurred three days before the eruption and then after the eruption abruptly decreased to levels below those observed before January 2015 (Fig. 3.3).

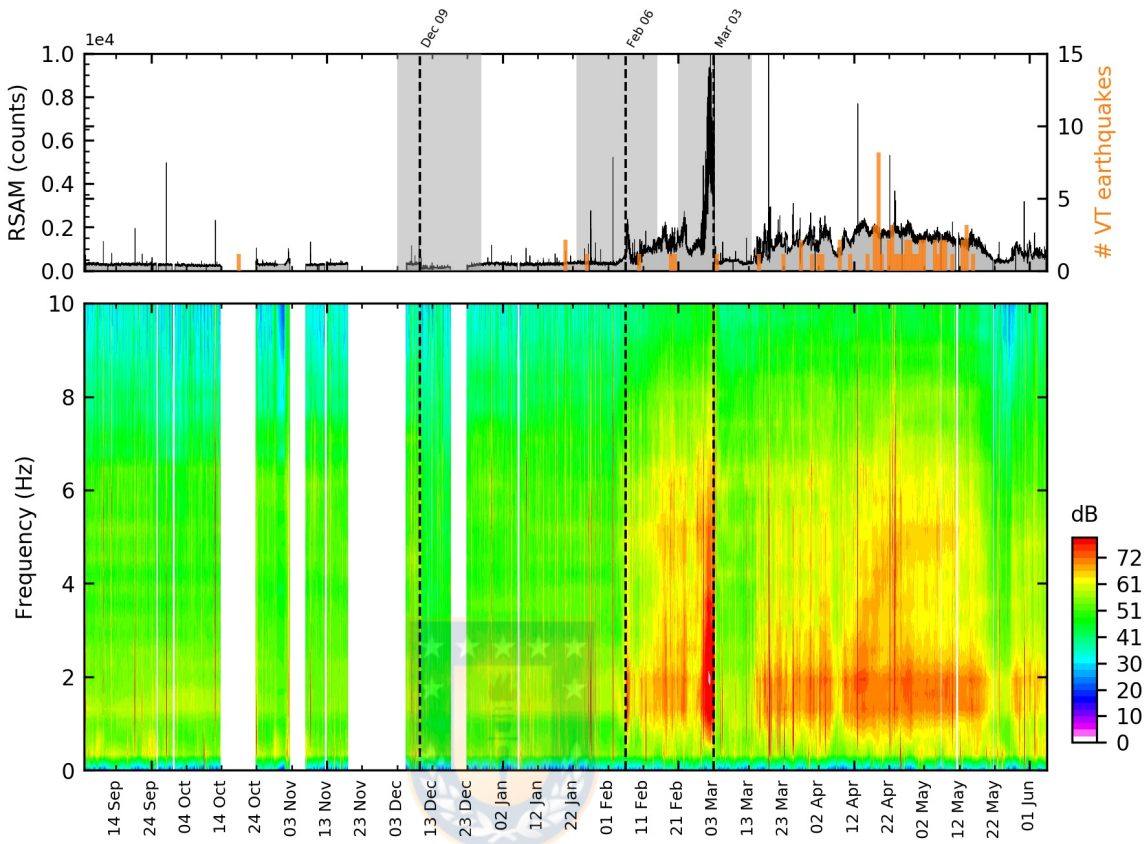

Figura 3.3: Panel A shows the Real-time Seismic Amplitude Measurement (RSAM) (Endo and Murray, 1991) between September 5th, 2014 and March 5th, 2015 for station VN2 (located at 3.2 km distance from Villarrica volcano cone). To compute the RSAM, we use a time window of 10 min length and a band-pass filter within $1 - 10$ Hz. The dashed black line marks the time of increased volcanic activity on February 6th and March 3rd, 2015 reported by Aiuppa et al. (2017). No instrument response correction was applied. Orange bars indicate the number of daily volcano-tectonic earthquakes around Villarrica volcano modified from Sielfeld et al. (2019). Panel B shows the seismic power spectrogram. To compute the spectrogram, we use a time window of 10 min length and a band-pass filter between 0,02 and 10,0 Hz. The amplitude of the volcanic tremor (i.e., $1{,}2 - 2{,}5$ Hz) shows an anomalously high amplitude on February 6th and sustained amplitudes above background continue until the eruption on March 3rd. Gray bands C, D and E indicate times of increased or decreased degassing activity at Villarrica volcano (details in Fig. 3.6). Black arrows show the continuous energy peaks related to the oceanic microseismicity and the volcanic tremor signal of Villarrica volcano. White spaces are caused by data gaps.

3.2.2. Noise Correlation Function

Coda waves are highly sensitive to seismic velocity changes in the medium between station pairs (Snieder and Hagerty, 2004; Sens-Schönfelder and Wegler, 2006).

We used the ambient seismic noise to retrieve the Noise Correlation Function (NCF) following the methodology proposed by Bensen et al. (2007). First, we cut all traces to 2 hours long waveforms. We rejected traces that: (1) show gaps larger than 12 minutes (10 % of the data), (2) the standard deviation of the 2 hours long trace is three times larger than the daily standard deviation, or (3) local seismicity occurred in the study area (based on the seismic catalog of Sielfeld et al. (2019)). Then, we removed the mean and linear trend. After correcting the instrument response, we applied a band-pass filter within $0{,}1 - 0{,}9$ Hz. This frequency band is characterized by multiple scattered seismic waves that sample the subsurface to about 2 km below the surface (Brenguier et al., 2007; Obermann et al., 2016). Later, we applied a 1-bit normalization (Larose et al., 2004; Cupillard et al., 2011) and spectral whitening within $0{,}1 - 0{,}9$ Hz. According to Mordret et al. (2016), the 1-bit normalization and spectral whitening reduce the influence of strong peaks of the noise spectrum and non-stationary sources of noise in the NCF. Finally, we computed the NCF between 2 hours-long traces using the vertical component for each station pair.

3.2.3. Coda Wave Interferometry

To monitor the temporal evolution of the activity of Villarrica volcano, we compared the coherent part of the strongly scattered coda waves using the stretching technique (Lobkis and Weaver, 2002; Grêt, 2003; Sens-Schönfelder and Wegler, 2006). Following Hadziioannou et al. (2009), seismic velocity perturbations between two re-

ceivers can be obtained by stretching or compressing a time window of the NCF by a stretching factor of $\Delta t/t$. The correlation coefficient (CC) between the "daily" and "reference" NCF is calculated for each $\Delta t/t$. For a homogeneous velocity perturbation, the value of $\Delta t/t$ that maximizes CC corresponds to the seismic velocity perturbation given by:

$$\Delta v/v = -\Delta t/t \tag{3.1}$$

In our case, we defined the "daily" NCF (φ_i^j) of each station pair i as the stack of at least eight NCFs of 2 hours-long associated with the day j. φ_i^j is rejected if there are fewer than eight NCFs. As the "daily" NCF are asymmetric (Fig. 3.4A), due to the anisotropy of the noise propagation directions (Obermann et al., 2013), we averaged the negative and positive lag times (Fig. 3.4B). Then, we defined the "reference" NCF (φ_i^{ref}) as the stack of "daily" NCFs between June 5th and November 5th, 2014. We chose this period because Villarrica volcano exhibited low amplitude seismic tremor and low levels of activity at the crater (Delgado et al., 2017; Johnson et al., 2018). Fig. 3.4A shows that "daily" NCFs were relatively stable during 2014. However, slight random fluctuations on "daily" NCFs began in February 2015 and lasted at least until June 2015. We found that four days before, and two days after, the eruption on March 3rd, 2015 the waveform and arrival times of coda waves were perturbed (Fig. 3.4B). Following Obermann et al. (2015) and Planès et al. (2015), these fluctuations are probably due to changes in the source of noise (e.g., increase of

tremor signal, explosions inside the volcano) or by changes in the elastic properties of the medium (e.g., injection of new magma, increase in magma degassing).

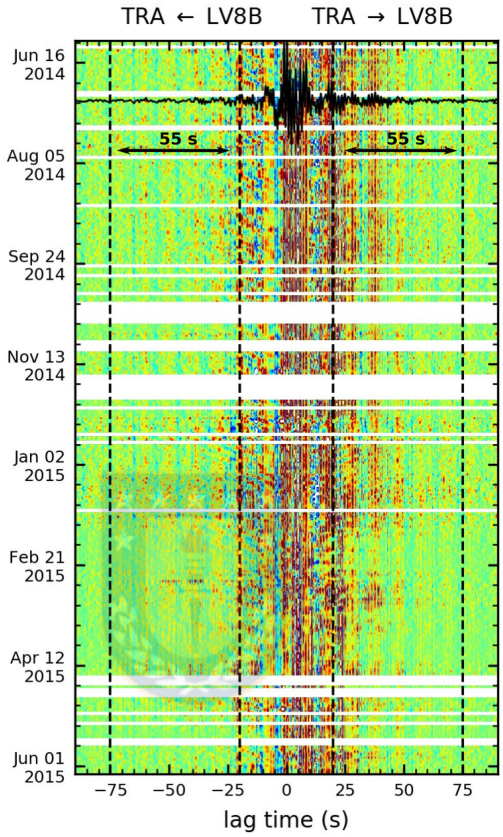

Figura 3.4: Noise Correlation Functions (NCFs) between stations LV8B and TRA. Panel A shows the negative and positive part of the "daily" NCFs between September 9th, 2014 and June 5th, 2015. The seismic data has been filtered between 0,1 Hz and 0,9 Hz. Dashed lines mark the lag times used for the stretching technique. White spaces are caused by gaps or low-quality seismic noise data. Orange-red colours indicate positive values of the NCFs while cyan-blue colours indicate negative values of the NCFs. Panel B compares the "daily" and "reference" NCF (continuous and dotted line, respectively) between February 25th and March 9th, 2015. Note that negative and positive lag times of the NCFs have been averaged. The orange line marks the "daily" NCF associated with the day of the eruption (March 3rd, 2015).

Next, we computed the stretching factor between $\Delta t/t = -2\,\%$ and $\Delta t/t = +2\,\%$. As we need to stretch coda waves that start after the surface wave arrivals (Obermann et al., 2013), we focused on lag times within $20 - 75$ s (dashed lines in Fig. 3.4A).

Since seismic velocity perturbations smaller than $\sim$ 0,2 % are not reliable (Sens-Schönfelder and Wegler, 2006), we smoothed the seismic velocity perturbations by defining a new "daily" NCF (ϕ_i^j) as the stack of a number of N "daily" NCFs:

$$\phi_i^j = \varphi_i^{(j-N,j)} \tag{3.2}$$

Fig. 3.5 shows that the correlation coefficient is significantly increased by incrementing the number of "daily" NCFs stacked on the new "daily" NCF. Finally, we computed the stretching factor using a "daily" NCF stacked by $N = 5$ "daily" NCFs. Also, as a quality criterion, we only consider as a reliable $\Delta v/v$ measurement if CC is greater than 0,5. In the case that CC is lower than 0,5, the velocity perturbation is shaded (Fig. 3.5).

3.3. Results

We found significant seismic velocity perturbations and low waveform coherence of strongly scattered coda waves occurring at times of changes in the amplitude of seismic tremor and observations of volcanic activity at the crater (Fig. 3.6). While perturbations in seismic velocity ($\Delta v/v$) reflect large-scale changes in the elastic parameters of the medium, the decorrelation coefficient (defined as $DC = 1 - CC$) is used to identify changes in the scattering properties of the medium (Haney et al., 2009; Obermann et al., 2013; Bennington et al., 2015). As seismic velocity perturba-

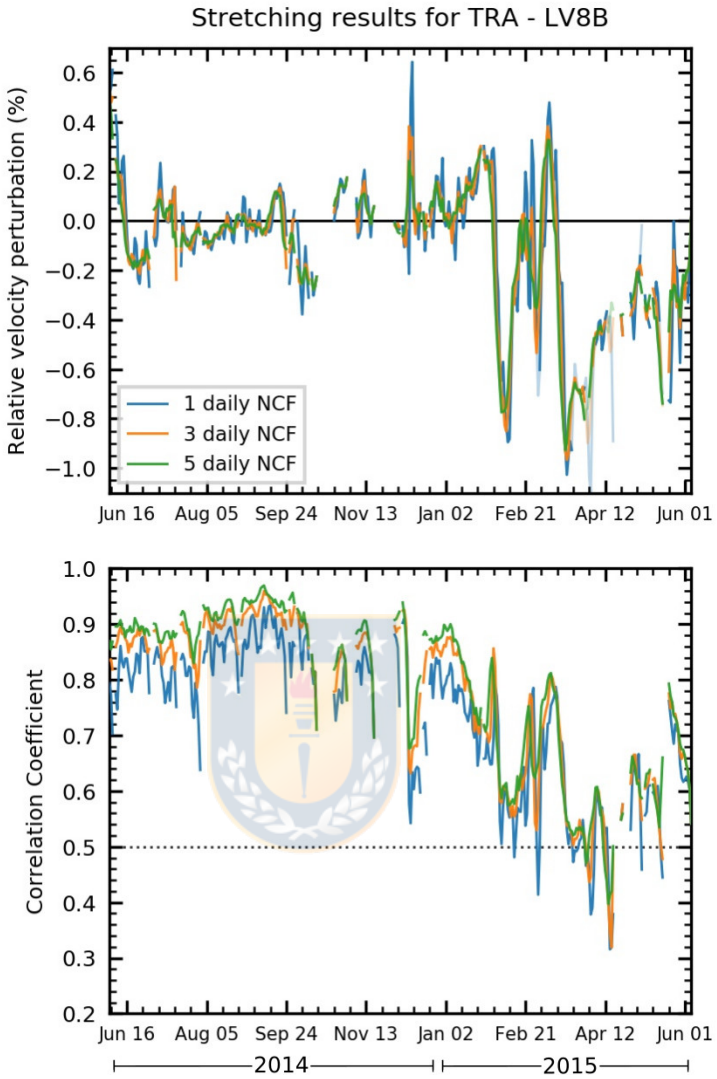

Figura 3.5: Example of seismic velocity perturbations ($\Delta v/v$) and correlation factor (CC) for the station pair LV8B−TRA. We show $\Delta v/v$ and CC measurements using a new "daily" NCF (ϕ_i^j) defined as the stack of $j-1$, $j-3$ and $j-5$ "daily" NCF φ_i^j. We shaded unresolved seismic velocity perturbations (i.e. $CC < 0{,}5$).

tions depend on the location of the receivers and intensity of the local perturbation below the surface (Obermann et al., 2013), we focus our attention on the results from station pairs TRA-LV8B, TRA-LV2S and LV8B-LV2S, which are at 15 km or less from the crater.

Seismic velocity perturbations and waveform decoherence were relatively small between June 16th and December 7th, 2014. During this time, we found values of $\Delta v/v < 0{,}15\,\%$ and $DC < 0{,}1$ on average (Fig. 3.6A and 3.6B, respectively). Later, the seismic velocity and waveform decoherence increased by $\Delta v/v \sim 0{,}3\,\%$ and $DC \sim 0{,}35$, on average, between December 7th and 10th, 2014 (Fig. 3.6C). On December 9th, an abrupt decrease in RSAM was observed on station VN2 (dashed line in Fig. 3.6C), which gradually returned to its mean level on December 24th, 2014. During January 2015, the seismic velocity perturbations fluctuated within $\pm 0{,}3\,\%$ (Fig. 3.6A). The waveform decoherence showed a linear increasing trend until January 30th, 2015 with values ranging within 0,2 to 0,4 on average (Fig. 3.6B). This range is wider than that observed before December 2014.

We found a significant decrease in seismic velocities ($0{,}75\,\%$ on average) and a strong waveform decoherence (within 0,4 to 0,8 on average) occurring between January 30th and February 8th, 2015 (Fig. 3.6D). On February 6th, an abrupt increase in RSAM was observed on station VN2 (dashed line in Fig. 3.6D), which is temporally coincident with an anomalously high degassing activity at the crater of Villarrica volcano (Aiuppa et al., 2017). Later, during the eight days previous to the paroxysmal eruption (i.e., within February 22th to March 3rd, 2015), the seismic velocity exhibits a decrease of $0{,}35\,\%$ on average, which is followed by an increase of $\sim 0{,}7\,\%$ after the eruption (Fig. 3.6E). Also, the waveform decoherence increased prior to the eruption, between 0,35 and 0,75 (gray band E in Fig. 3.6B). Then,

the waveform coherence was quickly recovered (i.e., $DC \sim 0{,}3$ on average) between March 3rd and 12th, 2015. These anomalies coincide with a significant increase in RSAM on February 28th, 2015; subsequently RSAM abruptly decreased after the eruption, reaching smaller values than those observed in the pre-eruptive phase (Fig. 3.6E).

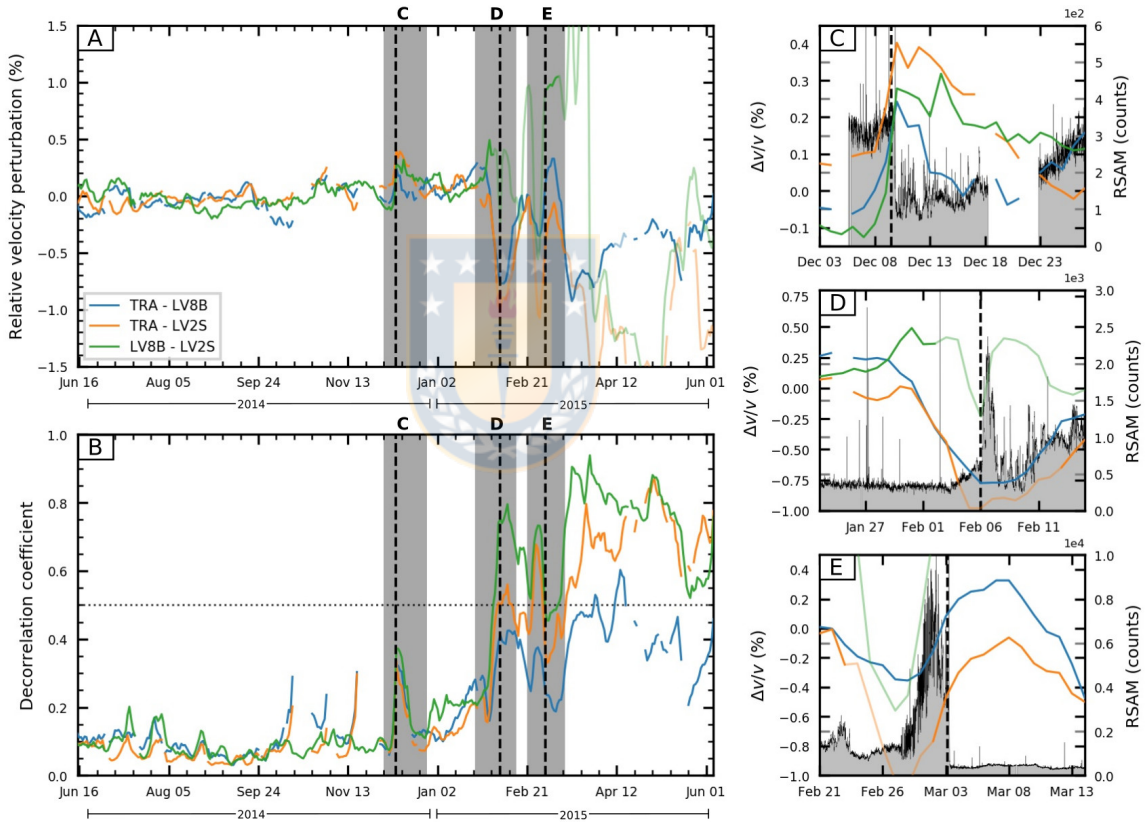

Figura 3.6: Seismic velocity perturbations ($\Delta v/v$) and decorrelation coefficient (DC) results (panels A and B, respectively) for station pairs TRA-LV8B, TRA-LV2S and LV2S-LV8B. The stations are located close to the Villarrica volcano (i.e. < 15 km distance). As a quality criterion, we shaded $\Delta v/v$ results associated with DC higher than 0.5 (dotted horizontal line in panel B). Gray bands C, D and E in panels A and B indicate times of increased or decreased degassing activity at Villarrica volcano from Aiuppa et al. (2017) and Johnson et al. (2018). Panels C, D and E show snapshots of RSAM from station VN2 to compare them with the seismic velocity perturbations obtained with ambient seismic noise.

3.4. Discussion and Conclusions

The analysis of coda wave time-shift and waveform decoherence can be useful for detecting small perturbations of the elastic medium surrounding a volcano. As the method has been successfully applied to Piton de la Fournaise (Duputel et al., 2008; Brenguier et al., 2011; Obermann et al., 2013; Sens-Schönfelder et al., 2014; Rivet et al., 2015) and to other volcanoes on the world (Snieder and Hagerty, 2004; Mordret et al., 2010; Ballmer et al., 2013; Bennington et al., 2015; Yukutake et al., 2016; Donaldson et al., 2017), we considered that the eruption on March 3rd, 2015 at Villarrica volcano is an ideal case to explore the capabilities of the ambient seismic noise technique as a monitoring tool.

We found significant seismic velocity perturbations and waveform decoherence of strongly scattered coda waves related to changes in the style and magnitude of the explosive outgassing activity at the crater of Villarrica volcano. Following Duputel et al. (2008), the observed decrease in seismic velocities and strong waveform decoherence between January 30th and the eruption on March 3rd, 2015 could be induced by inflation of cracks/dikes that are part of the deep plumbing system, and by changes in the mechanical properties of the magma due to the intrusion of new volatile-rich magma into the shallow plumbing system (Aiuppa et al., 2017; Johnson et al., 2018). The subsequent seismic velocity increase and recovery of waveform decorrelation between March 3rd and 12th, 2015 could be induced by depressurization

of the magma at depth and stabilization of the mechanical properties of the new magma. Between March 15th and June 5th, 2015 we observed significant and sustained waveform decoherence that reached higher values than those observed before the eruption on March 3rd, 2015. We considered that the seismic noise wavefield was not coherent enough to retrieve reliable seismic velocity perturbations during the dates after the eruption. According to Palma et al. (2008) and Johnson et al. (2018), these phenomena that occur within the plumbing system at depth are represented on the surface as oscillations of the lava lake level and variations in the frequency and magnitude of the outgassing activity. Our results show that the analysis of ambient seismic noise (particularly at low frequencies) can detect changes at depth before they become evident in the volcanic tremor (i.e., RSAM and power spetrogram) and in the activity observed within the crater (i.e., lava lake level, outgassing activity). Thus, we suggest that this technique could be used as a complementary monitoring technique that provides more information about changes in the activity of the volcano prior to eruption. Additionally, this technique would help to assess the risk management at basaltic open-vent systems such as Villarrica and surrounding populations.

Capítulo 4

CRUSTAL MODEL OF THE SOUTHERN CENTRAL ANDES DERIVED FROM AMBIENT SEISMIC NOISE RAYLEIGH-WAVE TOMOGRAPHY

Abstract

The distribution and the interconnection of magmatic bodies beneath volcanic arcs is key to asses volcanic hazard and eruptive processes taking place at convergent margins. We use ambient seismic noise Rayleigh-wave tomography to investigate the three-dimensional shear-wave crustal velocity structure of the Southern Central Andes between latitudes 33°S and 38°S (for the upper 30 km). We investigate the occurrence of magmatic reservoirs in the upper crust and show how their geometry is affected by local tectonics. The first prominent feature to be observed is the shear-wave velocity contrast between the volcanic arc and the faster fore-arc region. We

further identify areas of low shear-wave velocity from 3 km to 10 km depth beneath the volcanic arc, striking N-S, that we interpret as zones of fluid-rich crust, possibly characterised by confined regions of partial melts. Our results allow us to derive a model for the crustal structure of the Southern Central Andes. We propose that partial melts, marked by lower shear-wave velocity anomalies, are connected to shallower structural levels and reservoirs by brittle regions where dikes and exsolved fluids may propagate.

Published as: González-Vidal D.; Obermann, A.; Tassara, A.; Bataille, K.; Lupi, M. (2018), Crustal model of the Southern Andes derived from ambient seismic noise Rayleigh-wave tomography, *Tectonophysics, 744, 215-226.*

4.1. Introduction

In the southern part of central Chile the Nazca plate subduces obliquely with an average velocity of approximately 66 mm/yr beneath the South American plate (Fig. 4.1). This causes the development of a volcanic arc (herein Southern Central Andes - SCA) sub-parallel to the subduction trench between latitudes 33°S and 46°S. The region is affected by frequent large-magnitude earthquakes (e.g. M_w8.5 Concepción 1835, M_w8.2 Valparaiso 1906, M_w8.3 Talca 1928, M_w8.3 Chillán 1939, M_w9.5 Valdivia 1960, M_w8.8 Maule 2010) that may promote transient extensional faulting in the forearc (Ryder et al., 2012) and cause short-lived tectonic regimes in the volcanic arc (Lupi et al., 2014). This may lead to enhanced vertical migration of deep-seated fluids within the upper crust (Farías et al., 2011; Ryder et al., 2012; Pritchard et al., 2013; Lupi and Miller, 2014). Several seismic experiments have been conducted onshore and offshore Chile to shed light on the morphology of the subduction interface and the deformation of the overriding plate (Rietbrock et al., 2005; Groß et al., 2008; Haberland et al., 2009). Bohm et al. (2002) deployed 62 seismic stations from 36°S to 40°S to investigate the velocity structure of the upper lithosphere. Yuan et al. (2006) determined the crustal thickness beneath the volcanic arc (about 40 km) and Ward et al. (2013) performed a large-scale ambient noise tomography (also covering the region investigated here), retrieving shear-wave velocities from phase velocities, for the Central Andes up to 50 km depth. Such a tomography spanned from Peru (12°S)

to Southern Chile-Argentina (42°S). To date, regional investigations that shed light on the distribution of magmatic reservoirs in the upper crust beneath the volcanic arc are still missing. One of the major challenges hindering the development of regional-scale geophysical images of volcanic arcs is the logistically-complex accessibility of such regions.

The ambient noise tomography method is based on the inversion of dispersive surface-waves emerging from the cross-correlation of continuous seismic noise records between two stations (Lobkis and Weaver, 2002; Campillo and Paul, 2003; Shapiro and Campillo, 2004; Wapenaar, 2004). This method has been successfully applied in different settings (Shapiro et al., 2005; Ritzwoller et al., 2011; Singer et al., 2017). Recent studies on volcanoes, such as the Toba caldera, Sumatra (Stankiewicz et al., 2010), Piton de la Fournaise, La Réunion Island (Mordret et al., 2015), Snaefellsjökull volcano, Iceland (Obermann et al., 2016), and the Lusi hydrothermal system, Indonesia (Fallahi et al., 2017), have been able to highlight the distribution of shallow magmatic fluids using ambient seismic noise methods.

The volcanoes of the SCA are often perturbed by powerful seismic events promoting a dynamic evolution of the fluid distribution at depth. Spagnotto et al. (2015) recently showed that the M_w8.8 Maule earthquake triggered increased seismicity in the SCA. Bonali et al. (2015) pointed out how such a mega-thrust earthquake could cause stress changes on the volcanic arc and promote the vertical upwelling of fluids. The area investigated in the present study is in front of one of the regions most affec-

ted by the Maule earthquake in 2010. This M_w8.8 event caused a rupture zone about 500 km long spanning from 33,5°S to 38,5°S (Vigny et al., 2011; Wang et al., 2012; Moreno et al., 2012). To investigate the post-seismic deformation processes taking place after the Maule earthquake, a dense seismic network covering the region above the rupture zone was deployed by Lange et al. (2012). Farías et al. (2011) and Ryder et al. (2012) pointed out that the occurrence of NW-SE striking extensional faulting ($\sim$ 34,5°S in the forearc) was caused by relaxation occurring in the upper plate after the co-seismic slip of the M_w8.8 Maule earthquake. Lupi and Miller (2014), in agreement with Acocella et al. (2018), suggested that following large-magnitude megathrust earthquakes the tectonic regime affecting volcanic arcs in compressional margins may temporarily change, promoting transtensional and/or extensional tectonics. This is broadly in agreement with Pritchard et al. (2013) who detected about 15 cm of subsidence in five different volcanic systems in the SCA using InSAR data. Deformation occurred within the two years following the Maule earthquake. Such subsidence was proposed to be linked to seismically-promoted depressurization of the hydrothermal systems of the volcanic edifices. Similar behaviour was also observed in Japan after the M_w9.0 Tohoku 2011 earthquake (Takada and Fukushima, 2013).

The main goal of this work is to provide a picture of the crust beneath the volcanic arc in the SCA. Our Rayleigh-wave ambient noise tomography highlights magmatic reservoirs, sedimentary basins and batholitic complexes providing a conceptual model

for the region between latitudes 33°S and 38°S.

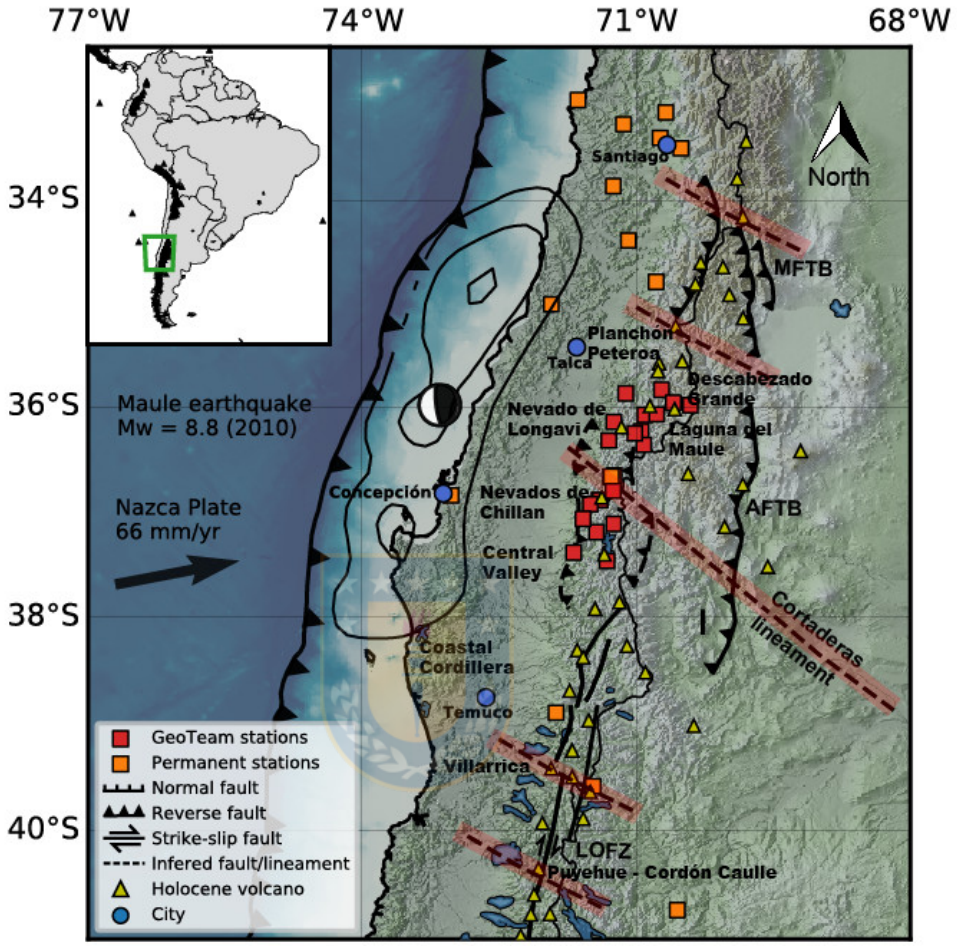

Figura 4.1: Simplified tectonic map of Southern Central Chile. The map shows the distribution of the volcanic centers and the large-scale fault systems of the Malagüe thrust-and-fold belts (MFTB), Agrio fold-and-thrust belts (AFTB) and Liquiñe-Ofqui fault zone (LOFZ), modified from Melnick and Echtler (2006), Cembrano and Lara (2009) and Radic (2010). Squares (colour-coded by network) show the distribution of seismic stations used for the seismic ambient noise tomography. Note that the GeoTeam network could not have been deployed across the Chilean-Argentinian border for permitting reasons. Black contours show the rupture area of Maule 2010 earthquake (M_w = 8,8) modified from Moreno et al. (2012).

4.2. Geological setting

The SCA is about 1500 km long and runs sub-parallel to the subduction trench. The tectonic evolution of the Southern Andes is characterised by a complex history controlled by convergent dynamics (e.g. James (1971); López-Escobar et al. (1995); Stern (2004); Ramos and Folguera (2005); Folguera et al. (2006); Kay et al. (2005); Melnick and Echtler (2006); Wang et al. (2007) and Ramos et al. (2014)). The oblique subduction of the Nazca plate beneath the South American plate causes strain partitioning in the overriding plate (Rosenau et al., 2006) leading to the development of a regional-scale transpressional fault zone, the Liquiñe-Ofqui fault zone (LOFZ) Cembrano and Lara (2009), and compressional thrust-and-fold belts (Malagüe - MFTB - and Agrio - AFTB in Fig. 4.1).

The LOFZ runs from $\sim$ 48°S to $\sim$ 38°S, strikes approximately N-S, and fades into the Agrio fold-and-thrust belt at around 38°S (Zamora-Valcarce et al., 2007). The Agrio fold-and-thrust belt merges northwards into the Malagüe thrust-and-fold belt (Giambiagi et al., 2012). The Coastal Cordillera and volcanic arc (Fig. 4.1) are distributed as margin-parallel mountain belts. Below the Coastal Cordillera the crustal thickness ranges from 20 km to 30 km (from West to East), while beneath the volcanic arc the crust is about 40 km thick (Yuan et al., 2006; Tassara and Echaurren, 2012). The Coastal Cordillera is characterised by plutonic and metamorphic units emplaced during the Late Paleozoic and Mesozoic (Willner et al.,

2009; Giambiagi et al., 2014; Cembrano and Lara, 2009). The volcanic arc is structured by Meso-Cenozoic volcano-sedimentary lithologies intruded by Mio-Pliocene plutons (Charrier et al., 2007; Hervé et al., 2007). The Central Valley (Fig. 4.1) is a graben-like depression between the Coastal Cordillera and the volcanic arc. The Central Valley can be divided into a few sedimentary basins characterised by Oligocene to Recent volcano-sedimentary units (Kay et al., 2005; Melnick and Echtler, 2006; Folguera et al., 2016).

The link between tectonics and volcanism in the SCA is complex and suggested to be strongly driven by crustal discontinuities that may be reactivated by supralithostatic pressures (Cembrano and Lara, 2009). Such basement lineaments (shown as red bands in Fig. 4.1) are proposed to strike NW-SE producing NW-elongated volcanic complexes (i.e. Nevados de Chillán) and NW-trending alignments of volcanic systems (i.e. Puyehue - Cordón Caulle, Villarrica - Quertupillán - Lanin, and Nevado de Longaví - Lomas Blancas - Resago). The most debated of such NW-trending lineaments in the SCA is possibly the Cortaderas lineament (Ramos and Kay, 2007; Stanton-Yonge et al., 2016; Tardani et al., 2016; Sielfeld et al., 2017). To date, little is known about the control that such structures exert on the emplacement of magmatic bodies and their morphology. Lupi and Miller (2014) proposed that megathrust earthquakes may unclamp such lineaments favoring the upwelling of deep-seated magmas. After the M_w8.8 earthquake some of the volcanic systems of the SCA went into unrest. These were the Planchón Peteroa, Nevados de Chillán,

Copahue, Cordón-Caulle, Villarrica and Calbuco volcanoes (Ovdas monthly reports, available on the website of Sernageomin: `http://www.sernageomin.cl/`).

4.3. Methods

4.3.1. Seismic Data

We used a total of 36 seismic stations spanning from $\sim$ 33°S to $\sim$ 41°S. Our experiment included the permanent Chilean seismic network consisting (in this region) of 15 broadband Trillium 120s/240s seismometers. In addition, a temporary network (GeoTeam) was installed from November 2013 to April 2015. The GeoTeam network was composed of 21 seismic stations provided by the GIPP (Geophysical Instrument Pool Potsdam, Germany). These are 11 broad-band Güralp ESP-C and 10 short-period Mark L4C seismometers recording with a sampling rate of 200 Hz. We deployed the sensors in the Chilean Andes to increase the resolution in the region of the volcanic arc (Fig. 4.1).

4.3.2. Cross-correlation computation

After instrumental response deconvolution, we downsampled the continuous waveforms to 5 Hz. We computed the cross-correlations for the vertical component of all station pairs following the work-flow of Bensen et al. (2007). This includes *i)* bandpass filtering between $1 - 40$ s; *ii)* clipping of 2 h signal segments showing am-

plitudes greater than 3 times the standard deviation of the daily trace; *iii)* spectral whitening of the amplitudes from 1 to 40 s; *iv)* one-bit amplitude normalization. We then stacked the vertical cross-correlation function for all the station pairs for the entire period of the experiment (i.e. 15 months, Fig. 4.2a) averaging positive and negative lag-times to enhance the signal-to-noise ratio of the emergent surface-waves (Yang et al., 2007; Mordret et al., 2014).

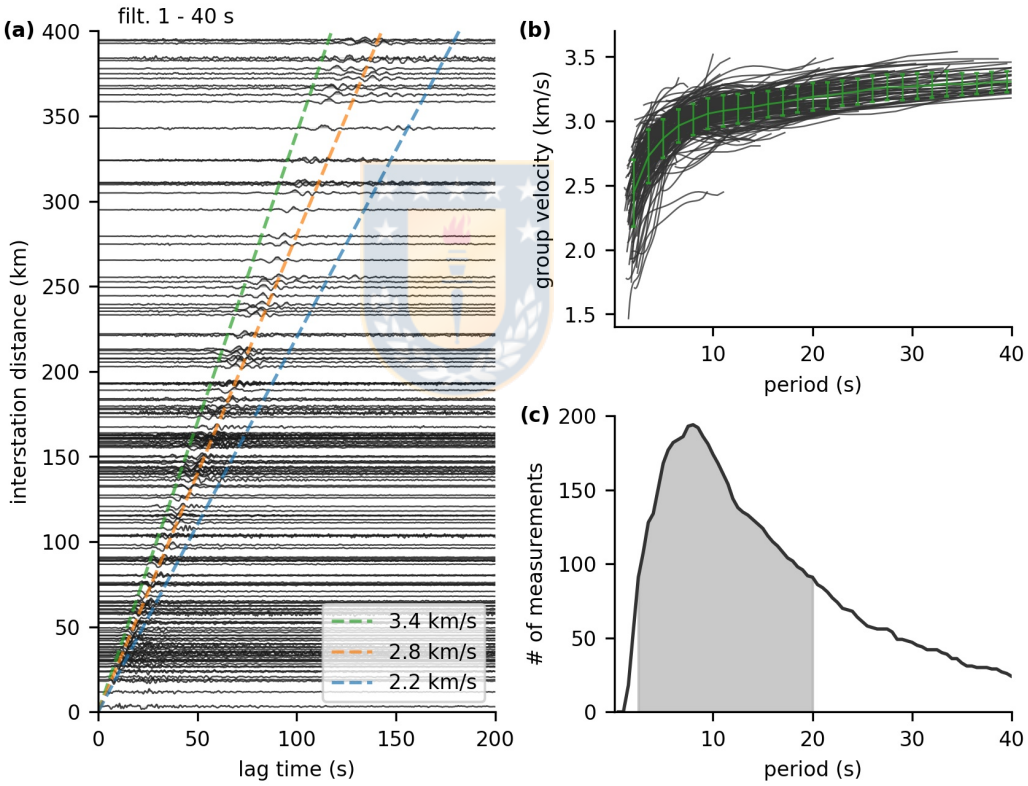

Figura 4.2: (a) Stacked cross-correlation functions of the vertical component of each station pair and sorted by inter-station distance (filter within $1-40$ s). (b) Black lines show the group-velocity dispersion curves for each cross-correlation function. Green bars show the standard deviation of each period. (c) Number of dispersion measurements for each period. For the Rayleigh-wave tomographic inversion we consider periods with greater than 90 measurements (grey area).

4.3.3. Rayleigh-wave dispersion measurements

We estimate the group-velocity dispersion curves with a frequency-time analysis for periods within $1-40$ s (Levshin et al., 1989; Ritzwoller et al., 1998) using a graphical user interface that involves visual validation of the dispersion curves (Mordret et al., 2014). Group velocities from inter-station distances smaller than 2 times the minimum wavelength, and a signal-to-noise ratio less than 2.5, were not considered. Fig. 4.2b shows the 228 dispersion curves calculated in this study. We observe a rapid increase of group-velocity from 3 to 8 s followed by a much smoother linear increase until 40 s. This second segment comprises group velocities between 2.8 km/s and 3.5 km/s. Fig. 4.2c shows the number of measurements as a function of period. We limit our analysis to reasonably covered period ranges with at least 90 dispersion measurements, which restricts us to periods ranging from 3 to 20 s. Such a period range coincides with the maximum sensitivity range of the short-period Mark L4C sensors.

4.3.4. 2-D tomographic inversion

We performed tomographic inversions of the group-velocity measurements for 171 periods between 3 and 20 s (with steps of 0.1 s) using the algorithms described by Barmin et al. (2001) and implemented by Mordret et al. (2013) in a Cartesian setting. The inversion involves a regularization function composed by a spatial Gaussian

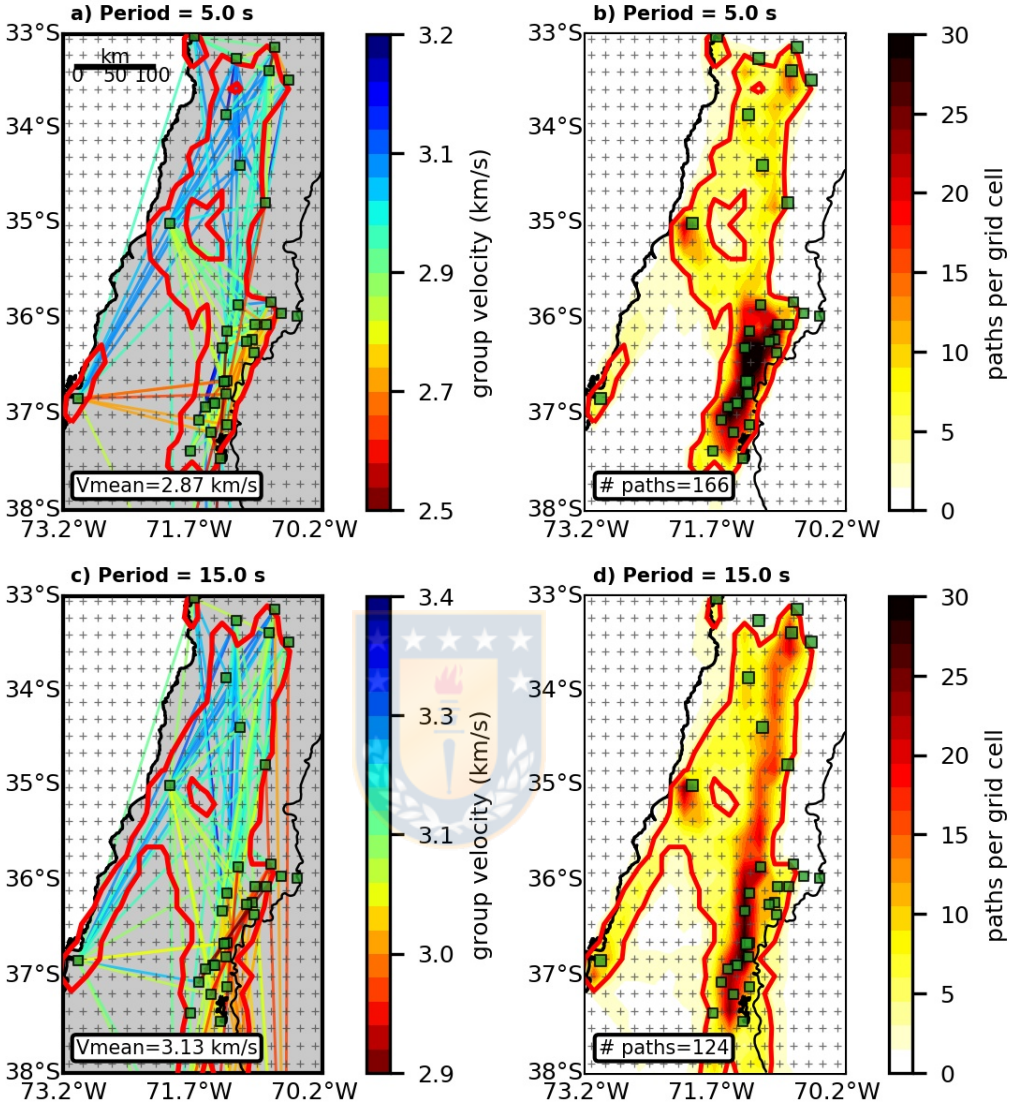

Figura 4.3: Ray path velocity of dispersion measurements (a, c) and path density (b, d) for 5 s (top panel) and 15 s period (bottom panel). The black crosses show the square grid of 20 km nodal separation. Green squares mark the location of seismic stations used in this study.

smoothing parameter ($\sigma = 50$ km), a damping parameter ($\alpha = 0{,}2$) and a constraint on the velocity perturbation amplitude which depends on the path density of each grid cell ($\beta = 0{,}8$). For the 2-D models we used $26 \times 52 = 1352$ cells with a regular

grid size of 20 km × 20 km (Fig. 4.3a, c). The relatively small grid size was chosen to allow higher resolution in the areas where we have a dense network (Fig. 4.3b, d). The initial model has a constant velocity that is taken as the mean group-velocity for each period. Following Mordret et al. (2015), we first invert a smoothed map that is used to identify and reject travel time perturbations greater than two standard deviations. Then, we use the remaining perturbations to produce the final 2-D group-velocity maps. Using the methodology of Ritzwoller et al. (1998) we evaluate the effect of different parameters on the resulting 2-D group-velocity maps. The chosen regularization parameters show a variance reduction greater than 75 % (VarRed in Fig. 4.4) and the resulting group-velocity maps are in agreement with the distribution of the main geological features in the region (i.e. intrusive bodies and sedimentary basins). The topography is not taken into account during the inversion procedure. In Fig. 4.4 the group-velocity maps are shown for 3 s, 5 s, 10 s and 15 s periods, with greater periods corresponding to an increased penetration depth. The mean velocity obtained from the inversion for the group-velocity maps increases linearly with period from 2.7 km/s to 3.1 km/s. To assess the depth range of the 2-D group-velocity maps we computed the depth sensitivity kernels following Herrmann (2013) using the averaged shear-wave velocity model obtained from the Rayleigh-wave ambient tomography. We found that Rayleigh-waves at periods of about 2.8 s are sensitive to the upper 3 km of the crust, while at 20 s, they are sensitive to about 30 km depth (Fig. 4.5c). Hence, we consider that the depth extension down to 30 km is reliable.

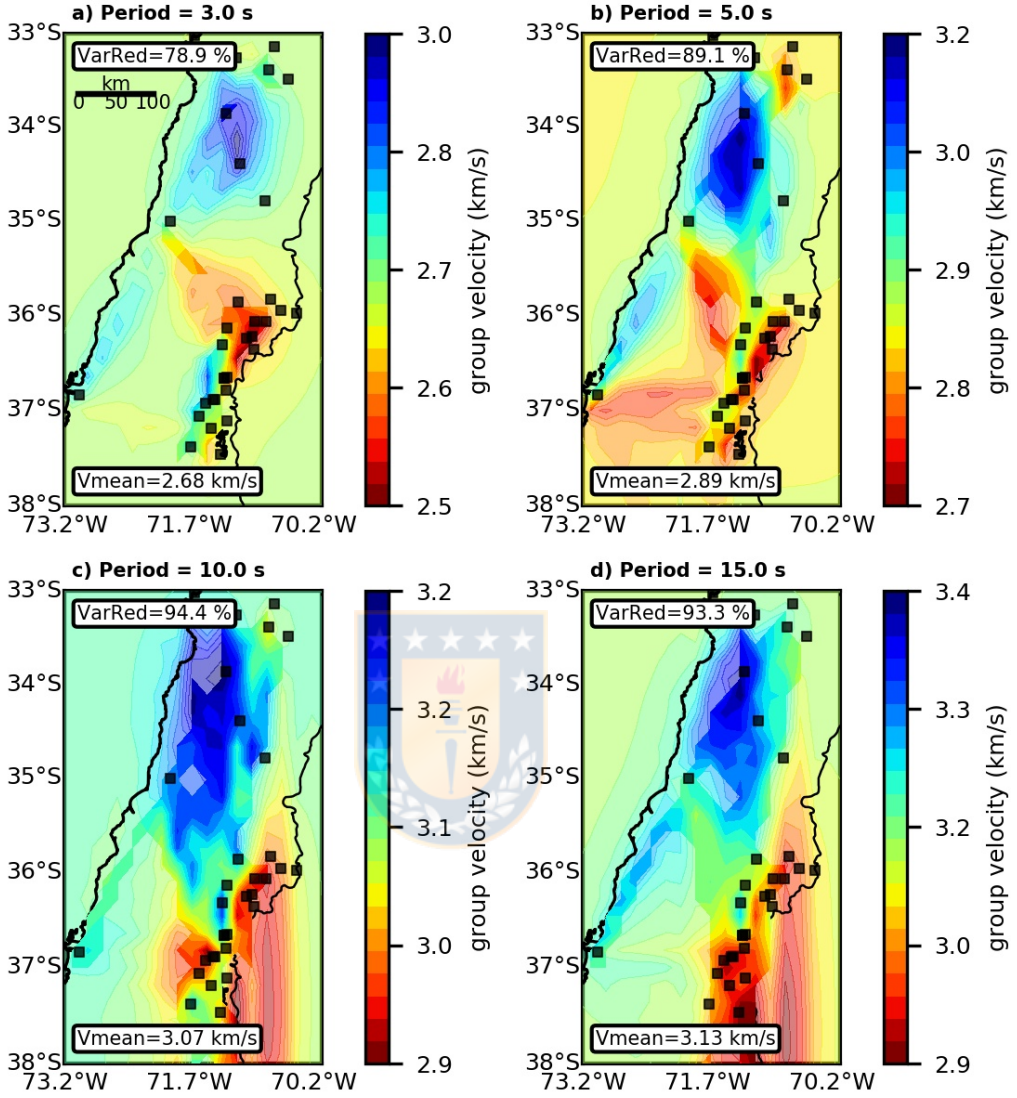

Figura 4.4: Group-velocity maps for (a) 3 s, (b) 5 s, (c) 10 s and (d) 15 s period obtained from the Rayleigh-wave tomographic inversion. We shaded the areas with < 4 ray paths per cell. We consider that a high variance reduction (i.e. VarRed$> 70\,\%$) indicates a good fit between the inverted model and the dispersion measurements.

4.3.5. Resolution test

We performed a resolution test to estimate the accuracy of the location and size of the velocity perturbations obtained from the tomographic inversion. We evalua-

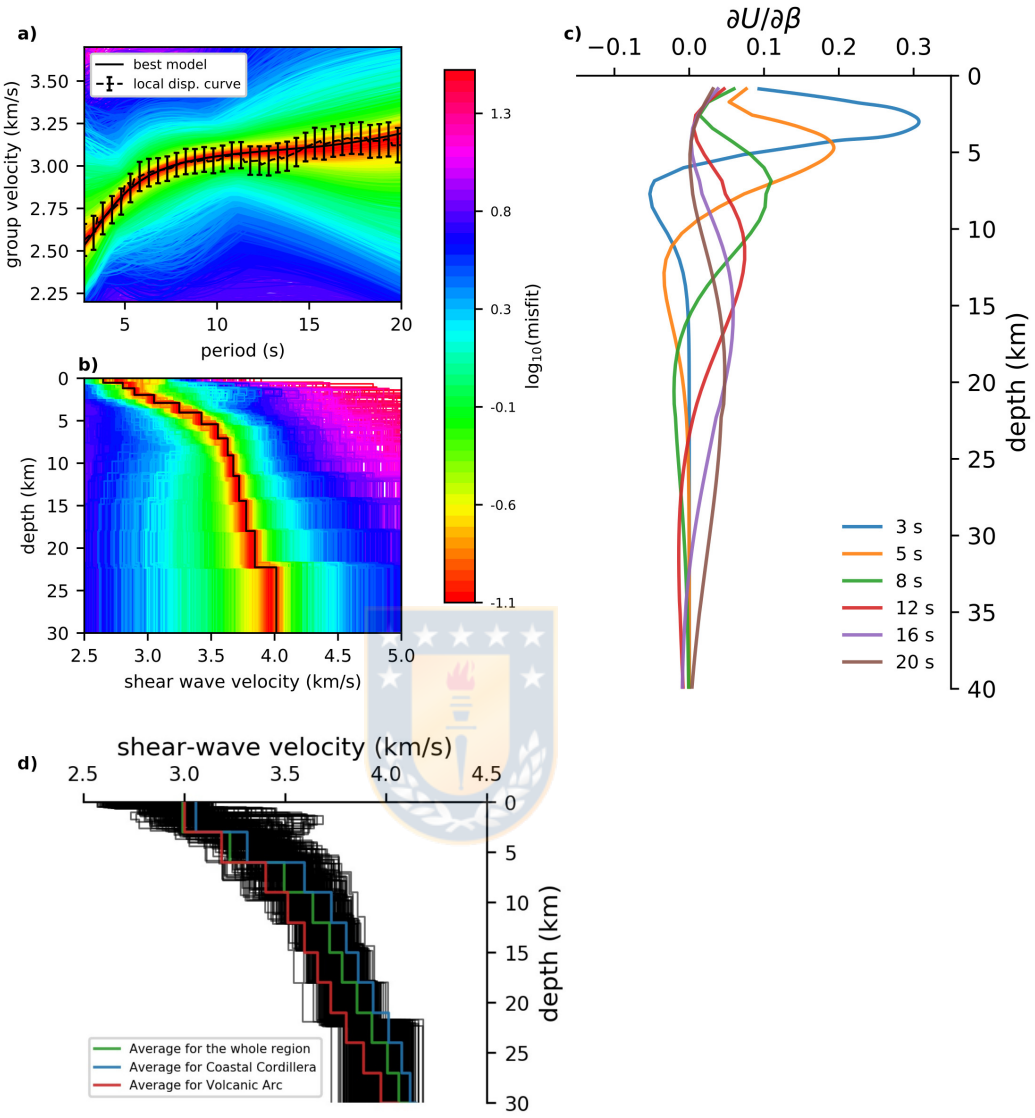

Figura 4.5: (a) Example of a local dispersion curve and (b) the inverted 1-D shear-wave velocity models (best model in black). The error bars indicate the standard deviation of the local dispersion curve. (c) Example of depth sensitivity kernels of group velocities (U) at 3 s, 5 s, 8 s, 12 s, 16 s and 20 s period with respect to shear-wave velocities (β). (d) All inverted velocity models (black), the average for the whole region (green), the Coastal Cordillera (blue) and the volcanic arc (red).

te the resolution matrix associated with each group-velocity map (Mordret et al., 2014). Each line of the resolution matrix represents the response of the tomographic inversion to a Delta function (spike) anomaly located in a given cell of the model.

The size, shape and location of the output spot given by the resolution matrix indicate how accurately the tomography is able to retrieve the velocity anomaly. We show the resolution shift that is the distance between the targeted grid cell and the centre of the ellipse (Fig. 4.6a, b). The ellipse is defined by the 40 % contour level of the maximum amplitude of the spike test resolution output (Mordret et al., 2014). Considering that the size of the regular square-based cells is 20 km, a resolution shift $\leq$ 40 km indicates that the anomaly is located within the targeted grid cell. Depending on the ray path coverage, the precision of the location and size of the velocity perturbation varies slightly across the model (Fig. 4.6). We also show the spatial resolution (Fig. 4.6c, d) that indicates the maximum reliable size of the retrieved anomalies. We consider that the shapes of the regional-scale geological features within the crust are well resolved at each period.

4.3.6. 3-D shear-wave velocity model

To obtain a three-dimensional shear-wave velocity (Vs) model of the crust, we constructed local dispersion curves for each grid cell of the model. Based on a neighbourhood algorithm (Sambridge, 1999; Mordret et al., 2014) we inverted each local dispersion curve to asses a 1-D Vs model following a power law dependency with depth for 15 homogeneous isotropic layers. Each Vs model is constrained by the velocity ($2{,}2 - 2{,}8$ km/s) and thickness ($2 - 4$ km) of the uppermost layer and the curvature of the profile ($\alpha = 0{,}01 - 0{,}12$). As P-wave velocity (Vp) and density of

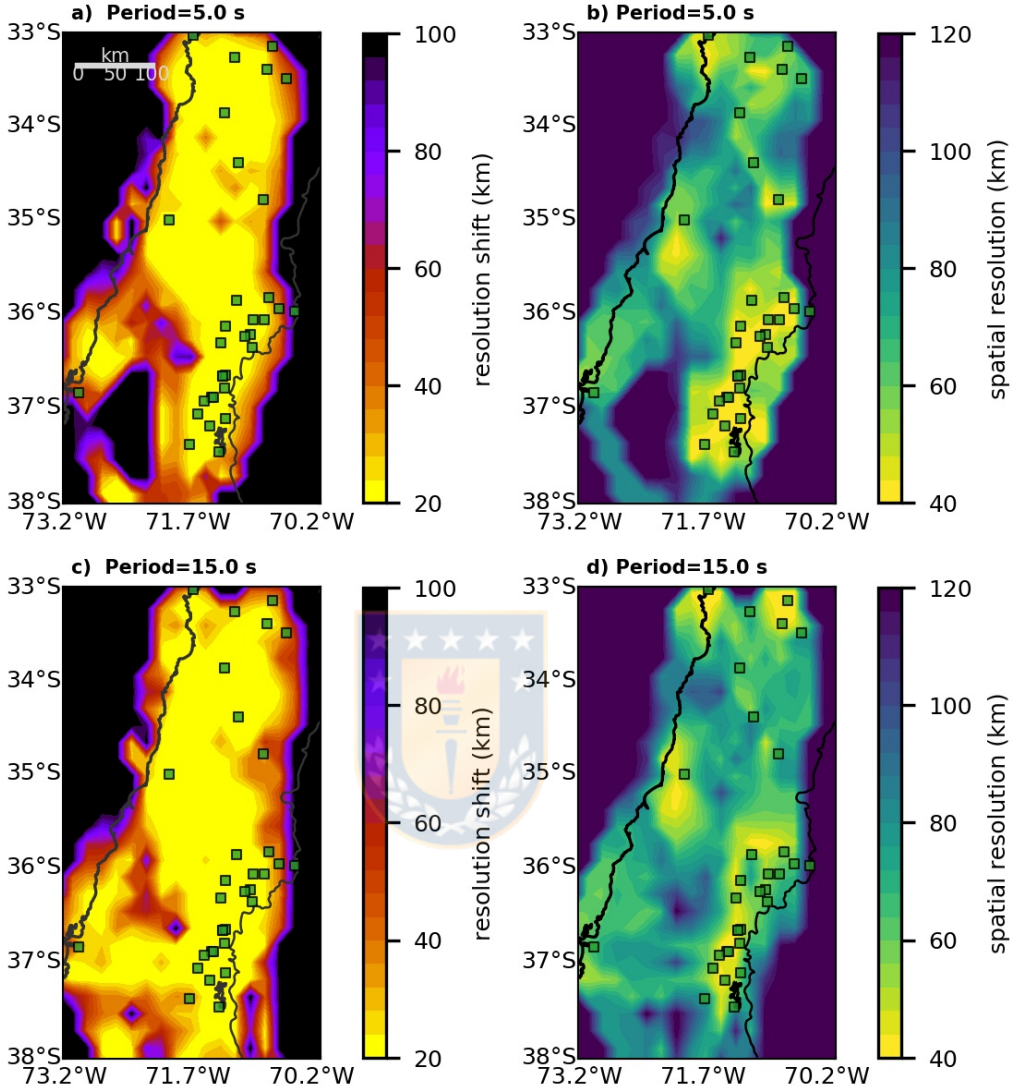

Figura 4.6: Resolution shift (a, c) and spatial resolution (b, d) for 5 s (top panels) and 15 s (bottom panels) period.

the crust are not known, Vp is assumed to directly depend on Vs using Poisson's ratio and the density is calculated from Vp using the relation $\rho = (Vp + 2{,}37)/2{,}81$ proposed by Obermann et al. (2016). A total of $21,000$ velocity models were sampled for each grid cell. First, we created 1000 velocity models and we computed the

misfit value between the synthetic and the observed dispersion curves (Fig. 4.5a and 4.5b). Next, we kept the best 500 velocity models to resample 5,000 new velocity models. This procedure was iterated 4 times to ensure the convergence at a global minimum (Fig. 4.5a, b). Finally, the best velocity models were linearly interpolated and smoothed resulting in a three-dimensional velocity model (Figs. 4.7, 4.8). The data from the 3-D inversion confirm the observations obtained from the 2-D group-velocity maps (Fig. 4.3). They also provide additional information about the depth and location of the anomalies. This procedure allows us to derive well-constrained shear-wave velocities between 2.7 and 4.5 km/s in the depth range between 3 and 30 km.

4.4. Results and discussion

We present a 3-D shear-wave velocity model for the upper 30 km of the SCA between 33°S and 38°S. Due to the configuration of the network the reliability of our data is approximately limited to the East by the Chilean-Argentinian border (see shaded regions in Figs. 4.7 and 4.8). The inversion shows the occurrence of shear-wave anomalies (both positive and negative) occurring at various depths (Fig. 4.7).

A region with a prominent positive shear-wave anomaly from about 4 % to 8 % corresponds to the region of the Coastal Cordillera (Figs. 4.7a, 4.8a, b, d). Such an anomaly strikes approximately N-S in the shallow crust becoming more trench-

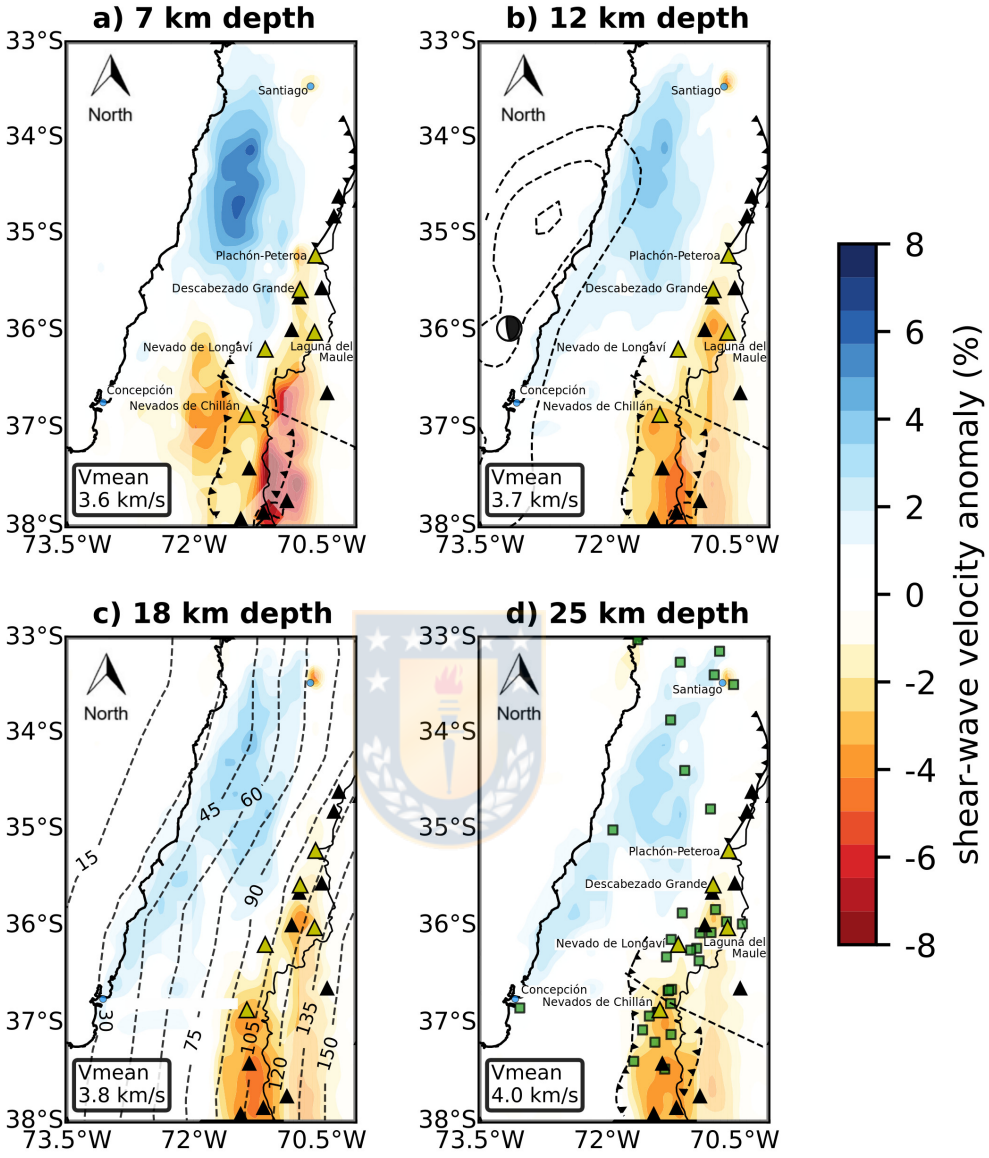

Figura 4.7: Horizontal sections of the shear-wave velocity model at (a) 7 km, (b) 12 km, (c) 18 km and (d) 25 km depth. The dashed black contours on (b) show the rupture area of Maule 2010 earthquake (M_w = 8,8) modified from Moreno et al. (2012). The dashed black contours on (c) show the subducting slab depth modified from Tassara and Echaurren (2012). The green squares on (d) show the location of the seismic stations used in this study. Refer to Fig. 4.1 for the symbols showing tectonic features. The areas where the raypath density is not enough to resolve shear-wave anomalies are shaded in light white.

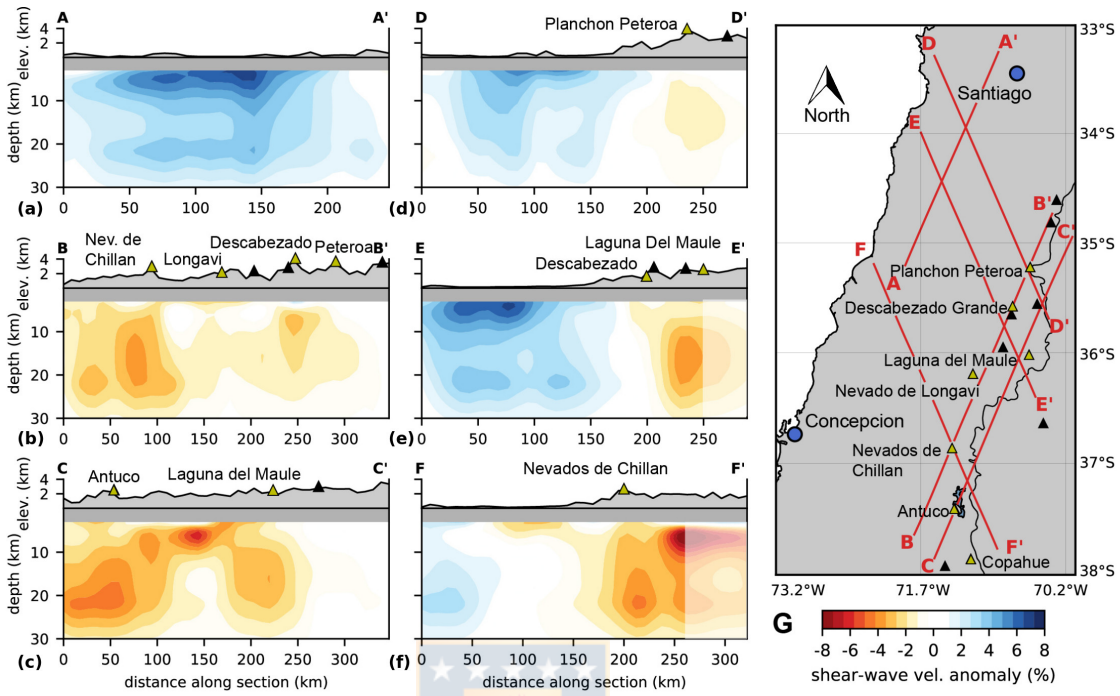

Figura 4.8: Vertical cross-sections of the shear-wave velocity model. Velocity anomalies were calculated with respect to the reference 1-D velocity model (green line in Fig. 4.5d). Note that we could not resolve crustal structures immediately below the volcanic arc (hence missing the upper part of the volcanic plumbing systems), we could invert from 2.8 s period only due to the low energy of the signal at higher frequencies. Fig. 4.5b shows that 3 s periods are sensitive to around ~ 4 km depth, therefore the upper 3 km of the models are shaded in gray. Black triangles point out the location of the volcanoes crossed by the cross-sections, the triangles with a yellow fill highlight volcanoes that may be taken as reference across the manuscript.

parallel at greater depths (Fig. 4.8a). The anomaly is prominent until about 7 km depth (Figs. 4.7a, 4.8a), can be tracked until about 37°S (Fig. 4.7b) and fades away at greater depths (to $0 - 4\,\%$). The shallow positive anomaly corresponds to the location where Mesozoic and late Paleozoic plutons crop out (Willner et al., 2009; Giambiagi et al., 2014; Cembrano and Lara, 2009). The inverted geophysical data match the mapped geological units providing better constraints on the geometries (and volumes) of the plutonic formations. Our tomography suggests that the intrusive

bodies cropping out at the surface may reach to at least $5 - 7$ km depth (Fig. 4.8a). We speculate that the deeper anomaly (less pronounced than the shallow one) may be caused by sub-horizontal sill-like units. These (possibly fractured) intrusive bodies seem to feed the shallow anomaly. The deeper bodies are marked by a less pronounced shear-wave anomaly as they may be pervaded by fluids migrating from the subduction interface located at about 35 km depth below the surface (Bohm et al., 2002; Haberland et al., 2009).

The negative shear-wave anomalies (-3 % to -5 %) are located at the base of the western flank of the volcanic arc (Fig. 4.7a) and are more pronounced in the region of the volcanic arc at about 37°S. Such a negative anomaly, broadly corresponding to the Central Valley region, may be associated with the sedimentary units making up the basins of this region (Kay et al., 2005; Melnick and Echtler, 2006; Folguera et al., 2016). East of the volcanic edifices (between 36°S and 38°S) the negative shear-wave anomalies reach up to -8 % and then disappear at greater than $\sim$ 25 km depth (Fig. 4.7). However, the ray-path coverage for this region (Fig. 4.3) is sparse. Only the western part of this region features a satisfying ray-path coverage. Fig. 4.3 shows the shaded area that should be interpreted with care.

Negative anomalies, associated with low shear-wave velocities measured in geological settings characterised by an overall low shear-wave velocity (such as in our case) may not appear to be prominent anomalies. The upper plates of convergent margins are fluid-rich and highly tectonized regions where fluids released by the

dehydration of the subducing slab may upwell and be trapped at various depths (Groß et al., 2008; Haberland et al., 2009). This may cause the average shear-wave velocity of such a crust to be lower than the one found in undeformed continental settings. In volcanic arcs, negative shear-wave anomalies have often been interpreted as magmatic reservoirs (e.g. Jay et al. (2012) and Fallahi et al. (2017)). Such negative anomalies are usually more pronounced compared to the one identified by our tomography. This may suggest alternative interpretations involving the occurrence of sedimentary basins (Arroucau et al., 2010; Pawlak et al., 2010) or hydrothermal systems (Obermann et al., 2016). However, sedimentary units buried at about 5 km depth may show a sub-horizontal elongation, while negative anomalies caused by hydrothermal systems of such size would not exist without the occurrence of magmatic bodies fuelling vigorous fluid circulation.

Our tomography points out that the volcanic arc features a N-S striking negative (-8 %) shear-wave anomaly between 3 km and 10 km depth (Fig. 4.7a). The resolution of our investigation does not allow us to distinguish possible shallow magmatic reservoirs inside (or just beneath) the volcanic edifice. However, these have been shown to exist in this region by previous studies (Miller et al., 2017). To investigate to what extent such anomalies may represent partial melts we compare our results with available data. Shear-wave velocities have been shown to be strongly affected by several factors, such as the amount of partial melt, water content and the thermal structure of the investigated region (Sato et al., 1989; Nelson et al., 1996; Takei,

1998; Hammond and Humphreys, 2002; Hacker and Abers, 2004; Priestley and McKenzie, 2013; Delph et al., 2017). Using a relationship between shear-wave velocity and melt fraction (Takei, 2002), Delph et al. (2017) calculated the percentage of partial melt for a regional-scale tomography in northern Chile (i.e. between latitudes $25° - 28°$S). The authors suggest that Vs larger than about 3,6 km/s may represent a crystallized body within the upper crust (i.e. < 20 km depth). The lowest Vs values pointed out in Fig. 4.6b are 2.7 km/s. If we assume similar upper crust conditions for the northern and southern Central Andes (Oncken et al., 2006; Tašárová, 2007; Tassara and Echaurren, 2012; Basset and Watts, 2015) we can speculate that the $-8\,\%$ shear-wave anomalies identified below the volcanic arc (with a lowest value of 2,7 km/s and typical values of $3{,}2 - 3{,}4$ km/s) are due to partial melts representing shallow large-scale magmatic reservoirs (Fig. 4.7).

The most pronounced anomaly extends N-S for about 80 km and about 30 km E-W, which implies a considerable volume of magma seated in the eastern part of the Andean Cordillera (Fig. 4.8b, c). This large volume of magma could be related to the western extension of the Payenia basaltic volcanic province that includes some of the largest active volcanoes in the region (Ramos and Folguera, 2011). When examined as a whole, the anomaly extends from 36°S to 38°S. Fig. 4.8b shows that the low shear-wave velocity region is still present, although less pronounced, at 18 km depth and continues down to the base of the region explored with our experiment. At depth, the negative shear-wave anomalies are bound on the sides by the thrust faults and

by the continuation of the Cortaderas lineament to the North (Fig. 4.7b). It must be noted that the most pronounced anomalies at 7 km depth are not continuous. This suggests the existence of separate magmatic reservoirs connected by buffer zones of partial melts, or fluid-rich geological units marked by negative shear-wave velocities.

The cross-sections (Fig. 4.8) point out that below the Planchón-Peteroa volcano the anomaly (less pronounced than in the South) is sub-circular in shape and centred at around 10-20 km depth (Fig. 4.8b). The Descabezado Grande features a more intense anomaly, shallower than 10 km, extending downwards until around 20 km depth. The deep magmatic reservoirs feeding the plumbing system of the Laguna del Maule and Nevados de Chillán volcanoes occur between 10 km and 20 km depth. We speculate that the distribution of fluids (including regions of partial melts) beneath the Nevados de Chillán volcano may be strongly tectonically-controlled (i.e. by the continuation of the Cortaderas lineament). The Nevados de Chillán is elongated according to a NW-trending lineament (the cones and craters constituting the volcanic edifice follow the same direction (Dixon et al., 1999)), and the prolongation of the Cortaderas lineament (that is not visible beneath the volcanic deposits of the SCA) approximately intercepts the Nevados de Chillán volcano. The profiles shown in Figs. 4.8c and 4.8f show a vertically elongated anomaly, as if it was confined in a broad deformation region (i.e. the extension of the Cortaderas lineament).

The conceptual model of the SCA is presented in Fig. 4.9 and supports the recently-proposed crustal structure of magmatic environments discussed by Cash-

man et al. (2017). The deeper negative shear-wave anomalies can be interpreted as melts segregating from the lower crust and upwelling by means of sheeted dikes. The magmas are temporarily stored in large-scale reservoirs located in the upper part of the lower crust. The geometry of such regions may be strongly controlled by the local stress field driving the emplacement of the magmatic bodies. Such deep-seated reservoirs could be viewed as large-scale ductile/molten regions given that the shear-wave anomalies are not extremely prominent at depth. These areas might be interconnected by colder and brittle-behaving regions (marked by less intense shear-wave anomalies) along which magmas and fluids are laterally transported from one reservoir to another. The model derived from the tomographic inversion shows that magmatic plumbing systems may cross the entire upper crust (i.e. vertical extension of more than 15 km) and extend laterally for about $20 - 30$ km. At shallower depths magmas are stored in large-scale reservoirs, not necessarily occurring beneath the volcanic edifices where the eruptive activity may take place. From here, magmas are then transferred to shallow reservoirs located below the volcanic cones. The resolution of our seismic experiment does not allow us to resolve such local and small-scale features. However, our results are in agreement with previous studies that have shown the occurrence of such reservoirs beneath the volcanic systems of the SCA (Miller et al., 2017).

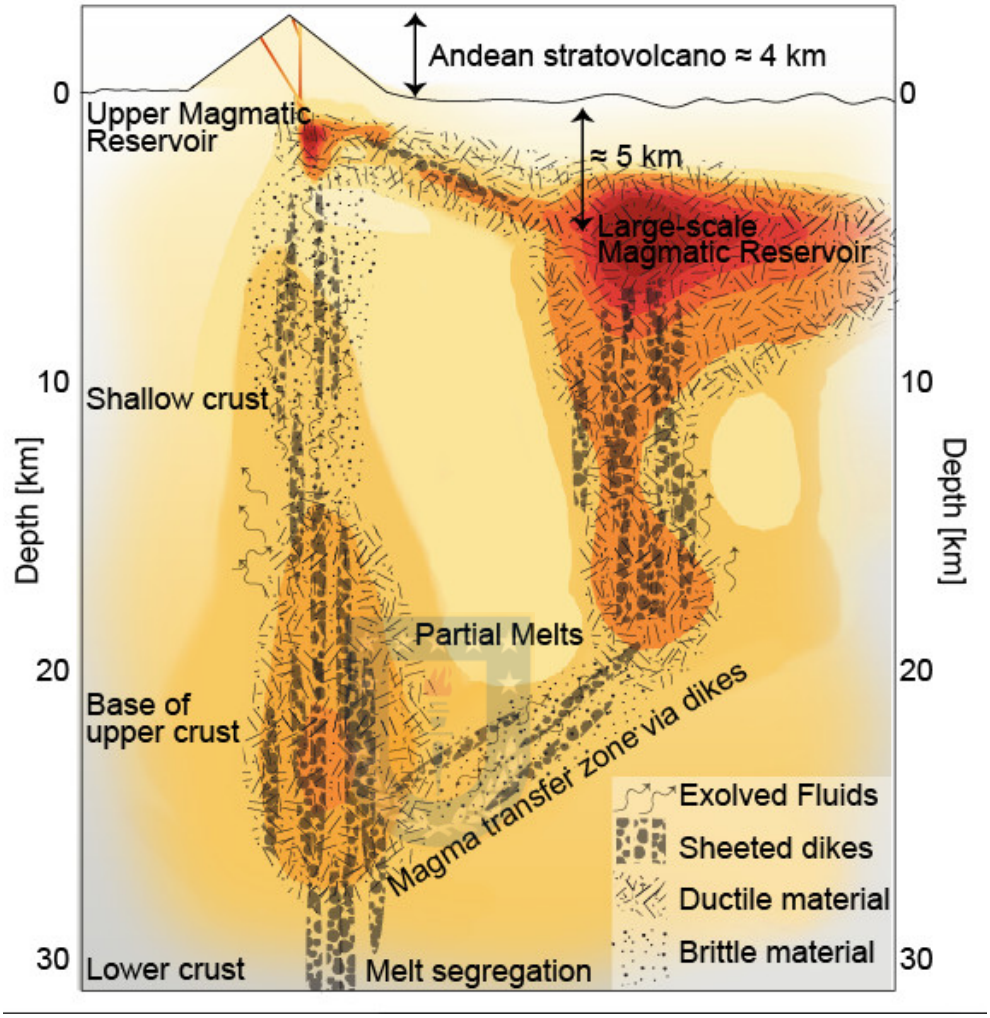

Figura 4.9: Conceptual model of the South Central Andes. The cartoon shows the occurrence of magmatic reservoirs located at different crustal levels. These ductile regions are connected by brittle-behaving units along which dikes intrude and fluids flow.

4.5. Conclusions

Using a network of 36 seismic stations deployed from 35,8°S to 37,5°S we measured group velocities from ambient noise correlations. We inverted for a three-dimensional shear-wave velocity model of the upper 30 km of crust below the Sout-

hern Central Andes. Our results indicate the occurrence of positive and negative shear-wave anomalies (±8 %). While we interpret positive shear-wave anomalies as intrusive bodies, the negative shear-wave anomalies may represent sedimentary basins and magmatic bodies. The former are located in the Central Valley between the western flanks of the Andes and the Coastal Cordillera. The latter occur beneath the volcanic arc and are interpreted as partial melts. A striking feature of the study is the occurrence of magmatic bodies in the eastern part of the Cordillera between 36,5°S and 38°S. We also show a strong control of the local tectonics on the morphology of the magmatic reservoirs.

The inversion allowed us to define a representative model of the Southern Central Andes. We show that magmas upwell from the lower crust and are stored at intermediate depths in large-scale regions of partial melts. From here magmas are transferred laterally and vertically along brittle-behaving regions (Fig. 4.9) where dikes intrude and connect magmatic reservoirs located in the middle crust. Large accumulations of magma occur at about 5 km depth and are not necessarily located beneath the volcanic edifices.

Capítulo 5

CONCLUSIONES GENERALES

En este trabajo, presentamos la aplicación de nuevas técnicas de análisis de datos sismológicos que utilizan el ruido sísmico ambiental para monitorear la estructura de velocidades sísmicas en la vecindad de volcanes, y estudiar la distribución espacial de las estructuras geológicas que afectan el desarrollo y comportamiento del arco volcánico.

En los capítulos 2 y 3, encontramos perturbaciones en la velocidad de ondas sísmicas ($\delta v/v$), en función del tiempo, que son consistentes con cambios en el nivel de actividad volcánica observados en la vecindad del volcán Láscar entre Febrero y Junio de 2013, y del volcán Villarrica entre Abril de 2014 y Junio de 2015. En general, los $\delta v/v$ observados tanto en volcán Lascar como en volcán Villarrica son del orden de magnitud entre 0,1 % y 1,0 %, lo cual es similar a lo observado con la misma técnica en otros volcanes activos en el mundo (Brenguier et al., 2008, 2011; Sens-Schönfelder and Wegler, 2011). Luego de analizar las señales obtenidas a partir de múltiples pares de estación distribuidos en la vecindad del volcán Lascar y Villarrica, encontramos que la magnitud y confiabilidad de los $\delta v/v$ obtenidos depende principalmente de

la banda de frecuencia en que se filtran las NCFs, la distancia y azimuth de la línea proyectada entre ambos receptores y el volcán, y además de la distribución y magnitud de las fuentes de ruido no estacionarias distribuidas alrededor de los receptores. Las NCFs filtradas a frecuencias mayores que 1,0 Hz están influenciadas principalmente por cambios hidrológicos de los primeros cientos de metros de la corteza y no necesariamente reflejan cambios en la actividad volcánica. Por otro lado, la banda de frecuencia entre 0,1 Hz y 0,9 Hz refleja perturbaciones que ocurren en promedio entre los primeros $\sim$ 10 km de profundidad, la cual es la profundidad donde se esperaría en que se almacenen los magmas en la parte superior de la corteza.

En el volcán Villarrica encontramos que el análisis del ruido sísmico ambiental entre 0,1 Hz y 0,9 Hz es capaz de detectar cambios en profundidad antes de que se vuelvan evidentes en el tremor volcánico y en la actividad observada en el crater. A pesar que el tremor volcánico contamina las NCF, nuestros resultados muestran que el ruido sísmico ambiental es una herramienta efectiva para monitorear cambios de velocidad en la vecindad del volcán Villarrica. De acuerdo con Ballmer et al. (2013), esto es posible cuando la localización espacial del tremor volcánico es estable en el tiempo. En general, los cambios de velocidad obtenidos en la vecindad de volcanes activos están asociados a procesos de inflación y deflación de la corteza debido a la intrusión o extrusión de magmas (lo cual no siempre es evidente a partir de observaciones InSAR y cGPS). Aplicar el análisis del ruido sísmico ambiental a múltiples bandas de frecuencia es útil para determinar la profundidad a la cual

se localizaría la fuente de inflación o deflación en la vecindad de un volcán, con el cual se puede implementar un sistema de monitoreo volcánico complementario a los métodos tradicionales. Estudios futuros involucran determinar el efecto que produce la topografía, cambios en la direccionalidad, amplitud y contenido espectral del tremor volcánico, la actividad antropogénica y el clima sobre las ondas de coda en la NCF.

En el Capítulo 4, se obtuvo una distribución espacial de $\delta v/v$ para los primeros 30 km de la corteza bajo el segmento del arco volcánico comprendido desde 35,5°S a 37,5°S. A partir de este modelo de velocidad, definimos un modelo representativo de la estructura de la corteza bajo este segmento del arco volcánico, en donde los magmas ascienden desde la corteza inferior y son almacenados como zonas de fundidos parciales de larga escala a profundidades intermedias. Desde ahí, los magmas son transportados lateral y verticalmente a través de zonas frágiles, donde los diques intruyen y conectan reservorios magmáticos localizados en la corteza superior. Nuestros resultados sugieren que la acumulación de fundidos o fluidos (e.g., magmas, fundidos parciales, fluidos hidrotermales, etc) ocurren aproximadamente a 5 km de profundidad y no necesariamente están localizados bajo el edificio volcánico.

Finalmente, sugerimos continuar con estudios enfocados en comprender aún mejor la naturaleza de las ondas que componen la coda de las señales obtenidas a partir del ruido sísmico ambiental en diferentes volcanes activos. Para ello, se requeriere procesar y analizar una gran cantidad de datos contínuos (i.e., de meses a años)

provenientes de redes de sensores distribuidos, idealmente, en la vecindad de un volcán activo con una geometría de anillos ubicados a un radio de $1-2$ km, $5-10$ km y $20-30$ km de distancia al edificio volcánico y con una densidad de al menos una estación por cada $10,000$ m^2 (i.e., al menos 25 estaciones en un área de 50 km $\times$ 50 km).

Bibliografía

Acocella, V., 2014. Structural control on magmatism along divergent and convergent plate boundaries: Overview, model, problems. Earth-Science Reviews 136, 226–288.

Acocella, V., Bellier, O., Sandri, L., Sébrier, M., Pramumijoyo, S., 2018. Weak Tectono-Magmatic Relationships along an Obliquely Convergent Plate Boundary: Sumatra, Indonesia. Frontiers in Earth Science 6.

Aiuppa, A., Bitetto, M., Francofonte, V., Velasquez, G., Parra, C.B., Giudice, G., Liuzzo, M., Moretti, R., Moussallam, Y., Peters, N., Tamburello, G., Valderrama, O.A., Curtis, A., 2017. A CO2-gas precursor to the March 2015 Villarrica volcano eruption. Geochemistry, Geophysics, Geosystems 18, 2120–2132.

Aki, K., Chouet, B., 1975. Origin of coda waves: Source, attenuation, and scattering effects. Journal of Geophysical Research 80, 3322–3342.

Arroucau, P., Rawlinson, N., Sambridge, M., 2010. New insight into Cainozoic sedimentary basins and Palaeozoic suture zones in southeast Australia from ambient noise surface wave tomography. Geophysical Research Letters 37, 1–6.

Asch, G., Schurr, B., Bohm, M., Yuan, X., Haberland, C., Heit, B., Kind, R., Woelbern, I., Bataille, K., Comte, D., Pardo, M., Viramonte, J., Rietbrock, A., Giese, P., 2006. Seismological Studies of the Central and Southern Andes, in: The Andes. Springer. chapter 21, pp. 443–457.

Ballmer, S., Wolfe, C.J., Okubo, P.G., Haney, M.M., Thurber, C.H., 2013. Ambient seismic noise interferometry in Hawaií reveals long-range observability of volcanic tremor. Geophysical Journal International 194, 512–523.

Barmin, M.P., Ritzwoller, M.H., Levshin, A.L., 2001. A Fast and Reliable Method for Surface Wave Tomography. Pure and Applied Geophysics 158, 1351–1375.

Basset, D., Watts, A.B., 2015. Gravity anomalies, crustal structure, and seismicity at subduction zones: 1. Seafloor roughness and subducting relief. Geochemistry, Geophysics, Geosystems 16, 1508–1540.

Behr, Y., Townend, J., Bowen, M., Carter, L., Gorman, R., Brooks, L., Bannister, S., 2013. Source directionality of ambient seismic noise inferred from three-component beamforming. Journal of Geophysical Research: Solid Earth 118, 240–248.

Bennington, N.L., Haney, M., De Angelis, S., Thurber, C.H., Freymueller, J., 2015. Monitoring changes in seismic velocity related to an ongoing rapid inflation event at Okmok volcano, Alaska. Journal of Geophysical Research: Solid Earth 120, 8439–8460.

Bensen, G.D., Ritzwoller, M.H., Barmin, M.P., Levshin, A.L., Lin, F., Moschetti, M.P., Shapiro, N.M., Yang, Y., 2007. Processing seismic ambient noise data to obtain reliable broad-band surface wave dispersion measurements. Geophysical Journal International 169, 1239–1260.

Bohm, M., Lüth, S., Echtler, H., Asch, G., Bataille, K., Bruhn, C., Rietbrock, A., Wigger, P., 2002. The Southern Andes between 36 and 40S latitude: Seismicity and average seismic velocities. Tectonophysics 356, 275–289.

Bonali, F.L., Tibaldi, A., Corazzato, C., 2015. Sensitivity analysis of earthquake-induced static stress changes on volcanoes: The 2010M¡inf¿w¡/inf¿8.8 Chile earthquake. Geophysical Journal International 201, 1868–1890.

Brenguier, F., Campillo, M., Hadziioannou, C., Shapiro, N.M., Nadeau, R.M., Larose, E., 2008. Postseismic relaxation along the San Andreas Fault at Parkfield from continuous seismological observation. Science 321, 1478–1481.

Brenguier, F., Clarke, D., Aoki, Y., Shapiro, N.M., Campillo, M., Ferrazzini, V., 2011. Monitoring volcanoes using seismic noise correlations. Comptes Rendus - Geoscience 343, 633–638.

Brenguier, F., Shapiro, N.M., Campillo, M., Nercessian, A., Ferrazzini, V., 2007. 3-D surface wave tomography of the Piton de la Fournaise volcano using seismic noise correlations. Geophysical Research Letters 34, 2–6.

Brock, B., Rivera, A., Casassa, G., Bown, F., Acuña, C., 2007. The surface energy balance of an active ice-covered volcano: Villarrica Volcano, southern Chile. Annals of Glaciology 45, 104–114.

Brooks, L.A., Townend, J., Gerstoft, P., Bannister, S., Carter, L., 2009. Fundamental and higher-mode Rayleigh wave characteristics of ambient seismic noise in New Zealand. Geophysical Research Letters 36, 2–6.

Campillo, M., 2006. Phase and correlation in 'random'seismic fields and the reconstruction of the green function. Pure and Applied Geophysics 163, 475–502.

Campillo, M., Paul, A., 2003. Long-range correlations in the diffuse seismic coda. Science 299, 547–549.

Cashman, K.V., Sparks, R.S.J., Blundy, J.D., 2017. Vertically extensive and unstable magmatic systems: A unified view of igneous processes. Science 355.

Cembrano, J., Lara, L., 2009. The link between volcanism and tectonics in the southern volcanic zone of the Chilean Andes: A review. Tectonophysics 471, 96–113.

Charrier, R., Pinto, L., Rodríguez, M.P., 2007. Tectonostratigraphic evolution of the Andean Orogen in Chile, in: The Geology of Chile. chapter 3, pp. 21–114.

Clements, T., Denolle, M.A., 2018. Tracking Groundwater Levels Using the Ambient Seismic Field. Geophysical Research Letters 45, 6459–6465.

Colombi, A., Chaput, J., Brenguier, F., Hillers, G., Roux, P., Campillo, M., 2014. On the temporal stability of the coda of ambient noise correlations. Comptes Rendus - Geoscience 346, 307–316.

Cupillard, P., Stehly, L., Romanowicz, B., 2011. The one-bit noise correlation: A theory based on the concepts of coherent and incoherent noise. Geophysical Journal International 184, 1397–1414.

Delgado, F., Lara, L., Pritchard, M.E., Ebmeier, S., Sciences, A., 2017. Recent unrest (2002 - 2015) imaged by space geodesy at the highest risk Chilean volcanoes : Llaima , Villarrica and Ca lbuco (Southern Andes). Journal of Volcanology and Geothermal Research 344, 270–288.

Delph, J.R., Ward, K.M., Zandt, G., Ducea, M.N., Beck, S.L., 2017. Imaging a magma plumbing system from MASH zone to magma reservoir. Earth and Planetary Science Letters 457, 313–324.

D'Hour, V., 2015. Medium change monitoring using ambient seismic noise and coda wave interferometry : examples from intraplate NE Brazil and the Mid-Atlantic Ridge . Medium change monitoring using ambient seismic noise and coda wave interferometry : examples from intraplat. Ph.D. thesis. Universidade Federal do Rio Grande do Norte.

Díaz, D., Brasse, H., Ticona, F., 2012. Conductivity distribution beneath Lascar volcano (Northern Chile) and the Puna, inferred from magnetotelluric data. Journal of Volcanology and Geothermal Research 217-218, 21–29.

Dixon, H.J., Murphy, M.D., Sparks, S.J., Chávez, R., Naranjo, J.A., Dunkley, P.N., Young, S.R., Gilbert, J.S., Pringle, M.R., 1999. The geology of Nevados de Chillán volcano, Chile. Revista geológica de Chile 26, 1–29.

Donaldson, C., Caudron, C., Green, R.G., Thelen, W.A., White, R.S., 2017. Relative seismic velocity variations correlate with deformation at Kīlauea volcano. Science Advances 3, e1700219.

Duputel, Z., Ferrazzini, V., Brenguier, F., Shapiro, N., Campillo, M., Nercessian, A., 2008. Real time monitoring of relative velocity changes using ambient seismic noise at the Piton de la Fournaise volcano (La Réunion) from January 2006 to June 2007. Journal of Volcanology and Geothermal Research 184, 164–173.

Endo, E.T., Murray, T.L., 1991. Volcanology a volcano monitoring and prediction tool. Bulletin of Volcanology 53, 533–545.

Fallahi, M.J., Obermann, A., Lupi, M., Karyono, K., Mazzini, A., 2017. The plumbing system feeding the Lusi eruption revealed by ambient noise tomography. Journal of Geophysical Research : Solid Earth 122.

Farías, M., Comte, D., Roecker, S., Carrizo, D., Pardo, M., 2011. Crustal extensional faulting triggered by the 2010 Chilean earthquake: The Pichilemu Seismic Sequence. Tectonics 30, 1–11.

Folguera, A., Naipauer, M., Sagripanti, L., Ghiglione, M.C., Orts, D.L., Giambiagi, L., 2016. Growth of the Southern Andes.

Folguera, A., Zapata, T., Ramos, V.A., 2006. Late Cenozoic extension and the evolution of the Neuquén Andes. Geological Society of America Special Pa.

Fournier, T.J., Pritchard, M.E., Riddick, S.N., 2010. Duration, magnitude, and frequency of subaerial volcano deformation events: New results from Latin America using InSAR and a global synthesis. Geochemistry, Geophysics, Geosystems 11.

Gassenmeier, M., Sens-Schönfelder, C., Eulenfeld, T., Bartsch, M., Victor, P., Tilmann, F., Korn, M., 2016. Field observations of seismic velocity changes caused by shaking-induced damage and healing due to mesoscopic nonlinearity. Geophysical Journal International 204, 1490–1502.

Giambiagi, L., Mescua, J., Bechis, F., Tassara, A., Hoke, G., 2012. Thrust belts of the southern Central Andes: Along-strike variations in shortening, topography, crustal geometry, and denudation. Bulletin of the Geological Society of America 124, 1339–1351.

Giambiagi, L., Tassara, A., Mescua, J., Tunik, M., Alvarez, P.P., Godoy, E., Hoke, G., Pinto, L., Spagnotto, S., Porras, H., Tapia, F., Jara, P., Bechis, F., García, V.H., Suriano, J., Maris-Moreiras, S., Pagano, S.D., 2014. Evolution of shallow and deep structures along the Maipo–Tunuyán transect (3340S): from the Pacific coast to the Andean foreland. Geological Society, London, Special Publications .

Grêt, A., 2003. Time-Lapse Monitoring with Coda Wave Interferometry. Ph.D. thesis. Colorado School of Mines.

Groß, K., Micksch, U., Araneda, M., Bataille, K., Bribach, J., Buske, S., Krawczyk, C.M., Lüth, S., Mechie, J., Schulze, A., Shapiro, S.A., Stiller, M., Wigger, P., Ziegenhagen, T., 2008. The reflection seismic survey of project TIPTEQ-the inventory of the Chilean subduction zone at 38.2 S. Geophysical Journal International 172, 565–571.

Haberland, C., Rietbrock, A., Lange, D., Bataille, K., Dahm, T., 2009. Structure of the seismogenic zone of the southcentral Chilean margin revealed by local earthquake traveltime tomography. Journal of Geophysical Research: Solid Earth 114, 1–17.

Hacker, B.R., Abers, G.A., 2004. Subduction Factory 3: An Excel worksheet and macro for calculating the densities, seismic wave speeds, and H2O contents of minerals and rocks at pressure and temperature. Geochemistry, Geophysics, Geosystems 5, 1525–2027.

Hadziioannou, C., Larose, E., Baig, A., Roux, P., Campillo, M., 2011. Improving temporal resolution in ambient noise monitoring of seismic wave speed. Journal of Geophysical Research: Solid Earth 116, 1–10.

Hadziioannou, C., Larose, E., Coutant, O., Roux, P., Campillo, M., 2009. Stability of Monitoring Weak Changes in Multiply Scattering Media with Ambient Noise Correlation: Laboratory Experiments. Acustical Society of America 125, 3688–3695.

Hammond, W.C., Humphreys, E.D., 2002. Upper mantle seismic wave attenuation: Effects of realistic partial melt distribution. Journal of Geophysical Research: Solid Earth 105, 10987–10999.

Haney, M.M., van Wijk, K., Preston, L.A., Aldridge, D.F., 2009. Observation and modeling of source effects in coda wave interferometry at Pavlof volcano. The Leading Edge 28, 554–560.

Hellweg, M., 1999. Seismic signals from Lascar Volcano. Journal of South American Earth Sciences 12, 123–133.

Henderson, S.T., Pritchard, M.E., 2013. Decadal volcanic deformation in the central andes volcanic zone revealed by InSAR time series. Geochemistry, Geophysics, Geosystems 14, 1358–1374.

Herrmann, R.B., 2013. Computer Programs in Seismology: An Evolving Tool for Instruction and Research. Seismological Research Letters 84, 1081–1088.

Hervé, F., Faundez, V., Calderón, M., Massonne, H.J., Willner, A.P., 2007. Metamorphic and plutonic basement complexes, in: The Geology of Chile. chapter 2, pp. 115–132.

Hill, D.P., Pollitz, F., Newhall, C., 2002. Earthquake-volcano interactions. Physics Today 55, 41.

Hillers, G., Ben-Zion, Y., Campillo, M., Zigone, D., 2015. Seasonal variations of seismic velocities in the San Jacinto fault area observed with ambient seismic noise. Geophysical Journal International 202, 920–932.

Hobiger, M., Wegler, U., Shiomi, K., Nakahara, H., 2014. Single-station cross-correlation analysis of ambient seismic noise: Application to stations in the surroundings of the 2008 Iwate-Miyagi Nairiku earthquake. Geophysical Journal International 198, 90–109.

James, D.E., 1971. Geological Society of America Bulletin Plate Tectonic Model for the Evolution of the Central Andes Plate Tectonic Model for the Evolution of the Central Andes. Geological Society of America Bulletin 82, 3325–3346.

Jay, J.A., Pritchard, M.E., West, M.E., Haney, M., Christensen, D., Haney, M., Minaya, E., Sunagua, M., McNutt, S.R., Zabala, M., 2012. Shallow seismicity, triggered seismicity, and ambient noise tomography at the long-dormant Uturuncu Volcano, Bolivia. Bulletin of Volcanology 74, 817–837.

Johnson, J.B., Watson, L.M., Palma, J.L., Dunham, E.M., Anderson, J.F., 2018. Forecasting the Eruption of an Open-Vent Volcano Using Resonant Infrasound Tones. Geophysical Research Letters 45, 2213–2220.

Kay, S.M., Godoy, E., Kurtz, A., 2005. Episodic arc migration, crustal thickening, subduction erosion, and magmatism in the south-central Andes. Bulletin of the Geological Society of America 117, 67–88.

Kimman, W.P., Campman, X., Trampert, J., 2012. Characteristics of seismic noise: Fundamental and higher mode energy observed in the northeast of the Netherlands. Bulletin of the Seismological Society of America 102, 1388–1399.

Lange, D., Tilmann, F., Barrientos, S.E., Contreras-Reyes, E., Methe, P., Moreno, M., Heit, B., Agurto, H., Bernard, P., Vilotte, J.P., Beck, S., 2012. Aftershock seismicity of the 27 February 2010 Mw 8.8 Maule earthquake rupture zone. Earth and Planetary Science Letters 317-318, 413–425.

Larose, E., Carriere, S., Voisin, C., Bottelin, P., Baillet, L., Gueguen, P., Walter, F., Jongmans, D., Guillier, B., Garambois, S., Gimbert, F., Massey, C., 2015. Environmental seismology: What can we learn on earth surface processes with ambient noise? Journal of Applied Geophysics 116, 62–74.

Larose, E., Derode, A., Campillo, M., Fink, M., 2004. Imaging from one-bit correlations of wideband diffuse wave fields. Journal of Applied Physics 95, 8393–8399.

Lecocq, T., Longuevergne, L., Pedersen, H.A., Brenguier, F., Stammler, K., 2017. Monitoring ground water storage at mesoscale using seismic noise: 30 years of continuous observation and thermo-elastic and hydrological modeling. Scientific Reports 7, 1–16.

Lepore, S., Markowicz, K., Grad, M., 2016. Impact of wind on ambient noise recorded by seismic array in northern Poland. Geophysical Journal International 205, 1406–1413.

Levshin, A.L., Yanovskaya, T.B., Lander, A.V., Bukchin, B.G., Barmin, M.P., Ratnikova, L.I., Its, E.N., 1989. Seismic surface waves in a laterally inhomogeneous earth.

Lobkis, O.I., Weaver, R.L., 2002. On the emergence of the Green's function in the correlations of a diffuse field. The Journal of the Acoustical Society of America 110, 3011–3017.

López-Escobar, L., Cembrano, J., Moreno, H., 1995. Geochemistry and tectonics of the Chilean Southern Andes. Andean Geology 22.

Lupi, M., Fuchs, F., Pacheco, J.F., 2014. Fault reactivation due to the M7.6 Nicoya earthquake at the Turrialba-Iraz volcanic complex, Costa Rica: Effects of dynamic stress triggering. Geophysical Research Letters 41, 4142–4148.

Lupi, M., Miller, S.A., 2014. Short-lived tectonic switch mechanism for long-term pulses of volcanic activity after mega-thrust earthquakes. Solid Earth 5, 13–24.

Mainsant, G., Larose, E., Brönnimann, C., Jongmans, D., Michoud, C., Jaboyedoff, M., 2012. Ambient seismic noise monitoring of a clay landslide: Toward failure prediction. Journal of Geophysical Research 117.

Margerin, L., Planès, T., Mayor, J., Calvet, M., 2016. Sensitivity kernels for coda-wave interferometry and scattering tomography: Theory and numerical evaluation in two-dimensional anisotropically scattering media. Geophysical Journal International 204, 650–666.

Melnick, D., Echtler, H.P., 2006. Morphotectonic and Geologic Digital Map Compilations of the South-Central Andes (36–42S), in: The Andes, pp. 565–568.

Miller, C.A., Williams-Jones, G., Fournier, D., Witter, J., 2017. 3D gravity inversion and thermodynamic modelling reveal properties of shallow silicic magma reservoir beneath Laguna del Maule, Chile. Earth and Planetary Science Letters 459, 14–27.

Mordret, A., Jolly, A.D., Duputel, Z., Fournier, N., 2010. Monitoring of phreatic eruptions using Interferometry on Retrieved Cross-Correlation Function from Ambient Seismic Noise: Results from Mt. Ruapehu, New Zealand. Journal of Volcanology and Geothermal Research 191, 46–59.

Mordret, A., Landes, M., Shapiro, N.M., Singh, S., Roux, P., Barkved, O.I., 2013. Near-surface study at the Valhall oil field from ambient noise surface wave tomography. Geophysical Journal International 193, 1627–1643.

Mordret, A., Landés, M., Shapiro, N.M., Singh, S.C., Roux, P., 2014. Ambient noise surface wave tomography to determine the shallow shear velocity structure at Valhall: Depth inversion with a Neighbourhood Algorithm. Geophysical Journal International 198, 1514–1525.

Mordret, A., Mikesell, T.D., Harig, C., Lipovsky, B.P., Prieto, G.A., 2016. Monitoring southwest Greenland's ice sheet melt with ambient seismic noise. Science Advances 2, 1–9.

Mordret, A., Rivet, D., Landès, M., Shapiro, N.M., 2015. Three-dimensional shear velocity anisotropic model of Piton de la Fournaise Volcano (La Réunion Island) from ambient seismic noise. Journal of Geophysical Research: Solid Earth 120, 406–427.

Moreno, M., Li, S., Melnick, D., Bedford, J.R., Baez, J.C., Motagh, M., Metzger, S., Vajedian, S., Sippl, C., Gutknecht, B.D., Contreras-Reyes, E., Deng, Z., Tassara, A., Oncken, O., 2018. Chilean megathrust earthquake recurrence linked to frictional contrast at depth. Nature Geoscience .

Moreno, M., Melnick, D., Rosenau, M., Baez, J., Klotz, J., Oncken, O., Tassara, A., Chen, J., Bataille, K., Bevis, M., Socquet, A., Bolte, J., Vigny, C., Brooks, B., Ryder, I., Grund, V., Smalley, B., Carrizo, D., Bartsch, M., Hase, H., 2012. Toward understanding tectonic control on the Mw 8.8 2010 Maule Chile earthquake. Earth and Planetary Science Letters 321-322, 152–165.

Nakata, N., Snieder, R., Kuroda, S., Ito, S., Aizawa, T., Kunimi, T., 2013. Monitoring a building using deconvolution Interferometry. I: Earthquake-data analysis. Bulletin of the Seismological Society of America 103, 1662–1678.

Nakata, N., Snieder, R., Tsuji, T., Larner, K., Matsuoka, T., 2012. Shear wave imaging from traffic noise using seismic interferometry by cross-coherence. Geophysics 76, 97–106.

Naranjo, J.A., Lara, L.E., 2004. August-September 2003 small vulcanian eruption at the Nevados de Chillán Volcanic Complex (3650'S), Southern Andes (Chile). Revista geológica de Chile 31, 1–9.

Nelson, K.D., Zhao, W., Brown, L.D., Kuo, J., Che, J., Liu, X., Makovsky, Y., Meissner, R., Mechie, J., Kind, R., Wenzel, F., Ni, J., Nabelek, J., Leshou, C., Tan, H., Wei, W., Jones, A.G., Booker, J., Unsworth, M., Hauck, M., Alsdorf, D., Ross, A., Cogan, M., Wu, C., Sandvol, E., Edwards, M., Nelson, K.D., Zhao, W., Brown, L.D., Kuo, J., Che, J., Liu, X., Klemperer, S.L., Makovsky, Y., Meissner, R., Mechie, J., Kind, R., Wenzel, F., Ni, J., Nabelek, J., Leshou, C., Tan, H., Wei, W., Jones, A.G., Booker, J., Unsworth, M., Kidd, W.S.F., Hauck, M., Alsdorf, D., Ross, A., Cogan, M., Wu, C., Sandvol, E., Edwards, M., 1996. Partially Molten Middle Crust Beneath Southern Tibet : Synthesis of Project INDEPTH Results Published by : American Association for the Advancement of Science Stable URL : http://www.jstor.org/stable/2890941 Accessed : 05-06-2016 10 : 29 UTC Your use of t. Science 274.

Nimiya, H., Ikeda, T., Tsuji, T., 2017. Spatial and temporal seismic velocity changes on Kyushu Island during the 2016 Kumamoto earthquake. Science Advances 3.

Obermann, A., Froment, B., Campillo, M., Larose, E., Planès, T., Valette, B., Chen, J.H., Liu, Q.Y., 2014. Seismic noise correlations to image structural and mechanical changes associated with the Mw 7 . 9 2008 Wenchuan earthquake. Journal of Geophysical Research: Solid Earth 119, 3155–3168.

Obermann, A., Kraft, T., Larose, E., Wiemer, S., 2015. Potential of ambient seismic noise techniques to monitor the St . Gallen geothermal site (Switzerland). Journal of Geophysical Research 120, 1–16.

Obermann, A., Lupi, M., Mordret, A., Jakobsdóttir, S.S., Miller, S.A., 2016. 3D-ambient noise Rayleigh wave tomography of Snæfellsjökull volcano, Iceland. Journal of Volcanology and Geothermal Research 317, 42–52.

Obermann, A., Planès, T., Larose, E., Campillo, M., 2013. Imaging preeruptive and coeruptive structural and mechanical changes of a volcano with ambient seismic noise. Journal of Geophysical Research: Solid Earth 118, 6285–6294.

Olivier, G., Brenguier, F., de Wit, T., Lynch, R., 2017. Monitoring the stability of tailings dam walls with ambient seismic noise. The Leading Edge 36, 350a1–350a6.

Oncken, O., Chong, G., Franz, G., Giese, P., Gotze, H.J., Ramos, V.A., Strecker, M.R., Wigger, P., 2006. The Andes. Springer.

Ortiz, R., Moreno, H., García, A., Fuentealba, G., Astiz, M., Pena, P., Sánchez, N., Tárraga, M., 2003. Villarrica volcano (Chile): Characteristics of the volcanic tremor and forecasting of small explosions by means of a material failure method. Journal of Volcanology and Geothermal Research 128, 247–259.

Pacheco, C., Snieder, R., 2005. Time-lapse travel time change of multiply scattered acoustic waves. The Journal of the Acoustical Society of America 118, 1300–1310.

Palma, J.L., Blake, S., Calder, E.S., 2011. Constraints on the rates of degassing and convection in basaltic open-vent volcanoes. Geochemistry, Geophysics, Geosystems 12.

Palma, J.L., Calder, E.S., Basualto, D., Blake, S., Rothery, D.A., 2008. Correlations between SO2 flux, seismicity, and outgassing activity at the open vent of Villarrica volcano, Chile. Journal of Geophysical Research: Solid Earth 113, 1–23.

Pavez, A., Remy, D., Bonvalot, S., Diament, M., Gabalda, G., Froger, J.L., Julien, P., Legrand, D., Moisset, D., 2006. Insight into ground deformations at Lascar volcano (Chile) from SAR interferometry, photogrammetry and GPS data: Implications on volcano dynamics and future space monitoring. Remote Sensing of Environment 100, 307–320.

Pawlak, A., Eaton, D.W., Bastow, I.D., Kendall, J.M., Helffrich, G., Wookey, J., Snyder, D., 2010. Crustal structure beneath Hudson Bay from ambient-noise tomography: implications for basin formation. Geophysical Journal International 184, 65–82.

Petit-Breuilh, M., Lobato, J., 1994. Analisis Comparativo de la Cronologia Eruptiva Historica de los Volcanes Llaima y Villarrica (38 - 39L.S.), in: VII Congreso Geológico Chileno, Concepción, Chile., pp. 366–370.

Planès, T., Larose, E., Rossetto, V., Margerin, L., 2015. Imaging multiple local changes in heterogeneous media with diffuse waves. The Journal of the Acoustical Society of America 137, 660–667.

Priestley, K., McKenzie, D., 2013. The relationship between shear wave velocity, temperature, attenuation and viscosity in the shallow part of the mantle. Earth and Planetary Science Letters 381, 78–91.

Pritchard, M.E., Jay, J.A., Aron, F., Henderson, S.T., Lara, L.E., 2013. Subsidence at southern Andes volcanoes induced by the 2010 Maule, Chile earthquake. Nature Geoscience 6, 632–636.

Pritchard, M.E., Simons, M., 2004. An InSAR-based survey of volcanic deformation in the southern Andes. Geophysical Research Letters 31, 1–42.

Radic, J.P., 2010. Las cuencas terciarias y su control en el volcanismo de los complejos chillan y copahue-callaqui (Sndes del Sur 36-39S). Andean Geology 37, 220–246.

Ramos, M.E., Folguera, A., Fennell, L., Giménez, M., Litvak, V.D., Dzierma, Y., Ramos, V.A., 2014. Tectonic evolution of the North Patagonian Andes from field and gravity data (39-40S). Journal of South American Earth Sciences 51, 59–75.

Ramos, V.A., Folguera, A., 2005. Tectonic evolution of the Andes of Neuquén: constraints derived from the magmatic arc and foreland deformation. Geological Society, London, Special Publications 252, 15–35.

Ramos, V.A., Folguera, A., 2011. Payenia volcanic province in the Southern Andes: An appraisal of an exceptional Quaternary tectonic setting. Journal of Volcanology and Geothermal Research 201, 53–64.

Ramos, V.A., Kay, S.M., 2007. Overview of the tectonic evolution of the southern Central Andes of Mendoza and Neuquén (35–39S latitude). Geological Society of America Special Pa, 1–17.

Richardson, J.P., Waite, G.P., 2013. Waveform inversion of shallow repetitive long period events at Villarrica Volcano, Chile. Journal of Geophysical Research: Solid Earth 118, 4922–4936.

Rietbrock, A., Haberland, C., Bataille, K., Dahm, T., Oncken, O., 2005. Studying the seismogenic coupling zone with a passive seismic array. Eos 86.

Ritzwoller, H., Ritzwoller, M.H., Levshin, A.L., 1998. Eurasian surface wave tomography; group velocities. Journal of Geophysical Research 103, 4839–4878.

Ritzwoller, M.H., Lin, F.C., Shen, W., 2011. Ambient noise tomography with a large seismic array. Comptes Rendus - Geoscience 343, 558–570.

Rivera, A., Zamora, R., Uribe, J., Wendt, A., Oberreuter, J., Cisternas, S., Gimeno, F., Clavero, J., 2015. Recent changes in total ice volume on Volcán Villarrica, Southern Chile. Natural Hazards 75, 33–55.

Rivet, D., Brenguier, F., Cappa, F., 2015. Improved detection of preeruptive seismic velocity drops at the Piton de La Fournaise volcano. Geophysical Research Letters 42, 6332–6339.

Rosenau, M., Melnick, D., Echtler, H., 2006. Kinematic constraints on intra-arc shear and strain partitioning in the southern Andes between 38S and 42S latitude. Tectonics 25, 1–16.

Ryder, I., Rietbrock, A., Kelson, K., Bürgmann, R., Floyd, M., Socquet, A., Vigny, C., Carrizo, D., 2012. Large extensional aftershocks in the continental forearc triggered by the 2010 Maule earthquake, Chile. Geophysical Journal International 188, 879–890.

Sambridge, M., 1999. Geophysical inversion with a neighbourhood algorithm-I. Searching a parameter space: Geophysical Journal International 138, 479–494.

Sánchez, P., Pérez-Flores, P., Arancibia, G., Cembrano, J., Reich, M., 2013. Crustal deformation effects on the chemical evolution of geothermal systems: the intra-arc Liquiñe–Ofqui fault system, Southern Andes. International Geology Review 55, 1384–1400.

Santibáñez, I., Yáñez, G., González, G., Cembrano, J., Costa, C., Arancibia, G., Marquardt, C., García-Pérez, T., 2019. Crustal faults in the Chilean Andes: geological constraints and seismic potential. Andean Geology 46, 32.

Sato, H., Sacks, I.S., Murase, T., 1989. The use of laboratory velocity data for estimating temperature and partial melt fraction in the low-velocity zone: comparison with heat flow and electrical conductivity studies. Journal of Geophysical Research 94, 5689–5704.

Scarpa, R., Tilling, R., 2006. Monitoring and Mitigation of Volcano Hazards. volume 164.

Sens-Schönfelder, C., 2008. Synchronizing seismic networks with ambient noise. Geophysical Journal International 174, 966–970.

Sens-Schönfelder, C., Pomponi, E., Peltier, A., 2014. Dynamics of Piton de la Fournaise volcano observed by passive image interferometry with multiple references. Journal of Volcanology and Geothermal Research 276, 32–45.

Sens-Schönfelder, C., Wegler, U., 2006. Passive image interferemetry and seasonal variations of seismic velocities at Merapi Volcano, Indonesia. Geophysical Research Letters 33, 1–5.

Sens-Schönfelder, C., Wegler, U., 2011. Passive image interferometry for monitoring crustal changes with ambient seismic noise. Comptes Rendus - Geoscience 343, 639–651.

Shapiro, N.M., Campillo, M., 2004. Emergence of broadband Rayleigh waves from correlations of the ambient seismic noise. Geophysical Research Letters 31, 8–11.

Shapiro, N.M., Campillo, M., Stehly, L., Ritzwoller, M.H., 2005. High-resolution surface-wave tomography from ambient seismic noise. Science 307, 1615–1618.

Sielfeld, G., Cembrano, J., Lara, L., 2017. Transtension driving volcano-edifice anatomy: Insights from Andean transverse-to-the-orogen tectonic domains. Quaternary International 438, 33–49.

Sielfeld, G., Lange, D., Cembrano, J., 2019. Intra-arc Crustal Seismicity: Seismo-tectonic Implications for the Southern Andes Volcanic Zone, Chile. Tectonics , 1–27.

Singer, J., Obermann, A., Kissling, E., Fang, H., Hetényi, G., Grujic, D., 2017. Along-strike variations in the Himalayan orogenic wedge structure in Bhutan from ambient seismic noise tomography. Geochemistry, Geophysics, Geosystems 18, 1483–1498.

Sippl, C., Schurr, B., Asch, G., Kummerow, J., 2018. Seismicity Structure of the Northern Chile Forearc. Journal of Geophysical Research : Solid Earth 123.

Snieder, R., 2006. The theory of coda wave interferometry. Pure and Applied Geophysics 163, 455–473.

Snieder, R., Hagerty, M., 2004. Monitoring change in volcanic interiors using coda wave interferometry: Application to Arenal Volcano, Costa Rica. Geophysical Research Letters 31.

Snieder, R., Wapenaar, K., 2010. Imaging with ambient noise. Physics Today 63, 44–49.

Sodoudi, F., Yuan, X., Asch, G., Kind, R., 2011. High-resolution image of the geometry and thickness of the subducting Nazca lithosphere beneath northern Chile. Journal of Geophysical Research: Solid Earth 116.

Spagnotto, S., Triep, E., Giambiagi, L., Lupari, M., 2015. Triggered seismicity in the Andean arc region via static stress variation by the MW=8.8, February 27, 2010, Maule earthquake. Journal of South American Earth Sciences 63, 36–47.

Stankiewicz, J., Ryberg, T., Haberland, C., Fauzi, N., Natawidjaja, D., 2010. Lake Toba volcano magma chamber imaged by ambient seismic noise tomography. Geophysical Research Letters 37, 3–7.

Stanton-Yonge, A., Griffith, W.A., Cembrano, J., St. Julien, R., Iturrieta, P., 2016. Tectonic role of margin-parallel and margin-transverse faults during oblique subduction in the Southern Volcanic Zone of the Andes: Insights from Boundary Element Modeling. Tectonics 35, 1990–2013.

Stern, C., 2004. Active Andean magmatism: its geologic and tectonic setting.

Takada, Y., Fukushima, Y., 2013. Volcanic subsidence triggered by the 2011 Tohoku earthquake in Japan. Nature Geoscience 6, 637–641.

Takei, Y., 1998. Constitutive mechanical relations of solid-liquid composites in terms of grain-boundary contiguity. Journal of Geophysical Research 103, 18183–18203.

Takei, Y., 2002. Effect of pore geometry on Vp/Vs: From equilibrium geometry to crack. Journal of Geophysical Research 107.

Tardani, D., Reich, M., Roulleau, E., Takahata, N., Sano, Y., Pérez-Flores, P., Sánchez-Alfaro, P., Cembrano, J., Arancibia, G., 2016. Exploring the structural controls on helium, nitrogen and carbon isotope signatures in hydrothermal fluids along an intra-arc fault system. Geochimica et Cosmochimica Acta 184, 193–211.

Tašárová, Z.A., 2007. Towards understanding the lithospheric structure of the southern Chilean subduction zone (36S-42S) and its role in the gravity field. Geophysical Journal International 170, 995–1014.

Tassara, A., Echaurren, A., 2012. Anatomy of the Andean subduction zone: Three-dimensional density model upgraded and compared against global-scale models. Geophysical Journal International 189, 161–168.

Tibaldi, A., 2008. Contractional tectonics and magma paths in volcanoes. Journal of Volcanology and Geothermal Research 176, 291–301.

Van Daele, M., Moernaut, J., Silversmit, G., Schmidt, S., Fontijn, K., Heirman, K., Vandoorne, W., De Clercq, M., Van Acker, J., Wolff, C., Pino, M., Urrutia, R., Roberts, S.J., Vincze, L., De Batist, M., 2014. The 600 yr eruptive history of Villarrica Volcano (Chile) revealed by annually laminated lake sediments. Bulletin of the Geological Society of America 126, 481–498.

Vigny, C., Socquet, A., Peyrat, S., Ruegg, K.C., Metois, M., Madariaga, R., Morvan, S., Lancieri, M., Lacassin, R., Campos, J., Carrizo, D., Bejar-Pizarro, M., Barrientos, S., Armijo, R., Aranda, C., Valderas-Bermejo, M.C., Ortega, I., Bondoux, F., Baize, S., Lyon-Caen, H., Pavez, A., Vilotte, J.P., Bevis, M., Brooks, B., Smalley, R., Parra, H., Baez, J.C., Blanco, M., Cimbaro, S., Kendrick, E., 2011. The 2010 Mw 8.8 Maule Megathrust Earthquake of Central Chile, Monitored by GPS. Science 332, 1417–1422.

Wang, K., Hu, Y., Bevis, M., Kendrick, E., Smalley, R., Barriga-Vargas, R., Lauría, E., 2007. Crustal motion in the zone of the 1960 Chile earthquake: Detangling earthquake-cycle deformation and forearc-sliver translation. Geochemistry, Geophysics, Geosystems 8, 1525–2027.

Wang, L., Shum, C., Simons, F.J., Tassara, A., Erkan, K., Jekeli, C., Braun, A., Kuo, C., Lee, H., Yuan, D.N., 2012. Coseismic slip of the 2010 Mw 8.8 Great Maule, Chile, earthquake quantified by the inversion of GRACE observations. Earth and Planetary Science Letters 335-336, 167–179.

Wapenaar, K., 2004. Retrieving the Elastodynamic Green's Function of an Arbitrary Inhomogeneous Medium by Cross Correlation. Physical Review Letters 93, 1–4.

Wapenaar, K., Draganov, D., Snieder, R., Campman, X., Verdel, A., 2010. Tutorial on seismic interferometry: Part 1 - Basic principles and applications. Geophysics 75, 75A195—-75A209.

Ward, K.M., Porter, R.C., Zandt, G., Beck, S.L., Wagner, L.S., Minaya, E., Tavera, H., 2013. Ambient noise tomography across the Central Andes. Geophysical Journal International 194, 1559–1573.

Weaver, R.L., Hadziioannou, C., Larose, E., Campillo, M., 2011. On the precision of noise correlation interferometry. Geophysical Journal International 185, 1384–1392.

Willner, A.P., Richter, P.P., Ring, U., 2009. Structural overprint of a late Paleozoic accretionary system in north-central Chile (34-35S) during post-accretional deformation. Andean geology 36.

Witter, J.B., Kress, V.C., Delmelle, P., Stix, J., 2004. Volatile degassing, petrology, and magma dynamics of the Villarrica Lava Lake, Southern Chile. Journal of Volcanology and Geothermal Research 134, 303–337.

Yang, Y., Ritzwoller, M.H., 2008. Characteristics of ambient seismic noise as a source for surface wave tomography. Geochemistry, Geophysics, Geosystems 9.

Yang, Y., Ritzwoller, M.H., Levshin, A.L., Shapiro, N.M., 2007. Ambient noise Rayleigh wave tomography across Europe. Geophysical Journal International 168, 259–274.

Yuan, X., Asch, G., Bataille, K., Bock, G., Bohm, M., Echtler, H., Kind, R., Oncken, O., Wolbern, I., 2006. Deep seismic images of the Southern Andes. Geological Society of America Special Pa, 61–72.

Yukutake, Y., Ueno, T., Miyaoka, K., 2016. Determination of temporal changes in seismic velocity caused by volcanic activity in and around Hakone volcano, central Japan, using ambient seismic noise records. Progress in Earth and Planetary Science 3.

Zamora-Valcarce, G., Zapata, T., del Pino, D., Ansa, A., 2007. Structural evolution and magmatic characteristics of the Agrio fold-and-thrust belt. Geological Society of America Special Pa, 125–145.

Apéndice A

Red GeoTeam (2013 - 2015)

La red temporal GeoTeam estuvo compuesta por 21 estaciones sismológicas (Fig. A.1A-B), donde se muestrearon registros sísmicos a 200 Hz. La red estuvo funcionado desde Noviembre de 2013 hasta Marzo de 2015 y consistió en 11 de sismógrafos banda ancha Guralp ESP-C y 10 periodo corto Mark L4C-3D. En este experiento registramos datos sísmicos contínuos sólo durante los periodos de verano Autral (i.e., desde Noviembre de 2013 a Marzo de 2014, y desde Noviembre de 2014 a Marzo de 2015). En la temporada de invierno Autral, las condiciones meteorológicas en alta montaña impidieron el correcto funcionamiento de los equipos electrónicos. Incluso, hubo lugares a los que no se pudo acceder para hacer el mantenimiento de la estación debido a la intensa caida de nieve y subidas de ríos. Además, el difícil acceso a las zonas remotas en las que fueron instaladas las estaciones sismológicas evitó que se lograran realizar mantenciones a las estaciones durante el invierno Austral. A continuación, se dan a conocer algunas recomendaciones al momento de seleccionar un sitio para instalar una estación sismológica:

- El terreno debe tener visibilidad del cielo en 360° para el funcionamiento óptimo del GPS.
- Evitar seleccionar un sitio que se encuentra a menos de 1 km de antenas o zonas que entren en resonancia debido al viento.
- Considerar los posibles cambios en los niveles de ríos y nieve en temporada de invierno al momento de planificar futuras mantenciones de la estación.
- Instalar el sismógrafo a $1-4$ metros de profundidad y sobre el basamento. En caso de no alcanzar el basamento, construir una base sólida de concreto (Fig. A.1C).
- Aislar térmicamente el sismógrafo, digitalizador y baterías.
- Instalar un sistema de telemetría para monitorear el correcto funcionamiento de la estación sismológica en tiempo real.
- En caso en que se presuman condiciones metereológicas extremas (i.e., temperaturas inferiores a 0°C y alta acumulación de nieve) será necesario considerar un sistema de calefacción integrado a la estación para proteger el digitalizador, batería(s) y panel(es) solar(es).

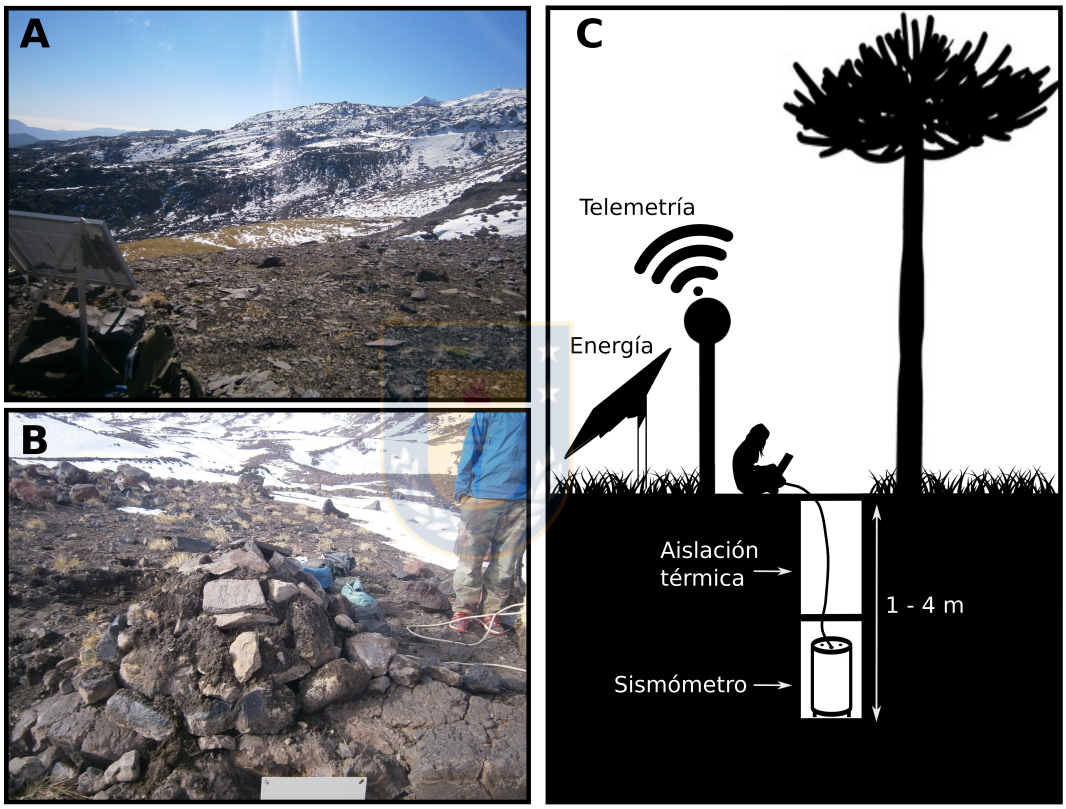

Figura A.1: (A) Foto del panel solar y (B) localización del sismógrafo de la estación BB03. (C) Dibujo representativo de los componentes de una estación sismológica: sismómetro, aislante térmico, fuente de energía y almacenamiento/telemetría digital de los datos. El sismómetro debe ser idealmente enterrado entre 1 y 4 metros de profundidad y aislado térmicamente para evitar el ruido proveniente de la superficie.